Measuring nickel masses in Type Ia supernovae using cobalt emission in nebular phase spectra

Michael J. Childress,[1,2][*] D. John Hillier,[3] Ivo Seitenzahl,[1,2] Mark Sullivan,[4]
Kate Maguire,[5] Stefan Taubenberger,[5] Richard Scalzo,[1] Ashley Ruiter,[1,2]
Nadejda Blagorodnova,[6] Yssavo Camacho,[7,8] Jayden Castillo,[1] Nancy Elias-Rosa,[9]
Morgan Fraser,[6] Avishay Gal-Yam,[10] Melissa Graham,[11] D. Andrew Howell,[12,13]
Cosimo Inserra,[14] Saurabh W. Jha,[8] Sahana Kumar,[11] Paolo A. Mazzali,[15,16]
Curtis McCully,[12,13] Antonia Morales-Garoffolo,[17] Viraj Pandya,[9,18] Joe Polshaw,[14]
Brian Schmidt,[1] Stephen Smartt,[14] Ken W. Smith,[14] Jesper Sollerman,[19]
Jason Spyromilio,[5] Brad Tucker,[1,2] Stefano Valenti,[12,13] Nicholas Walton,[6]
Christian Wolf,[1] Ofer Yaron,[10] D. R. Young,[14] Fang Yuan[1,2] and Bonnie Zhang[1,2]

Affiliations are listed at the end of the paper

ABSTRACT

The light curves of Type Ia supernovae (SNe Ia) are powered by the radioactive decay of ^{56}Ni to ^{56}Co at early times, and the decay of ^{56}Co to ^{56}Fe from $\sim$60 d after explosion. We examine the evolution of the [Co III] λ5893 emission complex during the nebular phase for SNe Ia with multiple nebular spectra and show that the line flux follows the square of the mass of ^{56}Co as a function of time. This result indicates both efficient local energy deposition from positrons produced in ^{56}Co decay and long-term stability of the ionization state of the nebula. We compile SN Ia nebular spectra from the literature and present 21 new late-phase spectra of 7 SNe Ia, including SN 2014J. From these we measure the flux in the [Co III] λ5893 line and remove its well-behaved time dependence to infer the initial mass of ^{56}Ni ($M_{\rm Ni}$) produced in the explosion. We then examine ^{56}Ni yields for different SN Ia ejected masses ($M_{\rm ej}$ – calculated using the relation between light-curve width and ejected mass) and find that the ^{56}Ni masses of SNe Ia fall into two regimes: for narrow light curves (low stretch $s \sim 0.7$–0.9), $M_{\rm Ni}$ is clustered near $M_{\rm Ni} \approx 0.4\,{\rm M}_\odot$ and shows a shallow increase as $M_{\rm ej}$ increases from $\sim$1 to 1.4 ${\rm M}_\odot$; at high stretch, $M_{\rm ej}$ clusters at the Chandrasekhar mass (1.4 ${\rm M}_\odot$) while $M_{\rm Ni}$ spans a broad range from 0.6 to 1.2 ${\rm M}_\odot$. This could constitute evidence for two distinct SN Ia explosion mechanisms.

Key words: supernovae: general.

1 INTRODUCTION

Type Ia supernovae (SNe Ia) were instrumental to the discovery of the accelerating expansion of the Universe (Riess et al. 1998; Perlmutter et al. 1999) and remain key tools for characterizing the precise cosmology of the Universe (Kessler et al. 2009; Sullivan et al. 2011; Betoule et al. 2014; Rest et al. 2014). Their cosmological utility is facilitated by both their intrinsic brightness ($M_B \sim -19$ mag at peak) and the relative uniformity of their peak brightnesses. More importantly, their luminosity diversity is tightly correlated with the width of the optical light curve (Phillips 1993). The physical origin of this width–luminosity relation (WLR) has long been a subject of debate and is intimately tied to the progenitor system of SNe Ia and the physical mechanism that triggers the explosion.

SNe Ia are widely believed to result from the thermonuclear disruption of a carbon–oxygen (CO) white dwarf (WD; Hoyle & Fowler 1960), which has recently been supported observationally for the very nearby SN 2011fe (Nugent et al. 2011; Bloom et al. 2012). The CO-rich material in a WD is supported against gravitational collapse by electron degeneracy pressure. A stable isolated WD lacks the internal pressure and temperature necessary to fuse CO to heavier elements (but see Chiosi et al. 2015). In SNe Ia, this balance is upset by interaction with some binary companion,

[*] E-mail: mjc@mso.anu.edu.au

which triggers runaway nuclear fusion of the CO material to heavier elements, particularly iron group elements (IGEs) dominated by radioactive ^{56}Ni. The energy from fusion unbinds the star and ejects material at $\sim 10^4$ km s^{-1}. As the ejecta expand, the decay of ^{56}Ni to ^{56}Co (with half-life of $t_{1/2} = 6.08$ d) releases energy into the ejecta which powers the optical light curve of the SN for the first few weeks after explosion (Colgate & McKee 1969), including the luminous peak. At later epochs ($t \gtrsim 60$ d past explosion), the SN Ia light curve is powered by ^{56}Co decay to ^{56}Fe (with half-life of $t_{1/2} = 77.2$ d). Thus, understanding the origin of the trigger mechanism and the amount of ^{56}Ni produced in the explosion would reveal the critical elements that make SNe Ia such excellent cosmological tools.

The nature of the CO-WD binary companion is directly responsible for the event that triggers the SN Ia explosion. One possible scenario is the single-degenerate (SD; Whelan & Iben 1973; Nomoto 1982) scenario in which a CO-WD steadily accretes from a non-degenerate (main-sequence or giant-like) companion until the central density of the WD exceeds the critical density for carbon ignition (e.g. Gasques et al. 2005) as the mass approaches the Chandrasekhar mass ($M_{\rm WD} \approx 1.4\,M_\odot$). In this scenario, the WLR has been proposed to arise from stochastic variations in the time at which the nuclear burning front within the exploding WD transitions from sub-sonic to super-sonic – the so-called deflagration-to-detonation transition (DDT; e.g. Blinnikov & Khokhlov 1986; Kasen & Woosley 2007; Röpke & Niemeyer 2007; Kasen, Röpke & Woosley 2009; Sim et al. 2013). Variations in the time of the DDT result in different amounts of ^{56}Ni being produced, yielding different peak magnitudes and light-curve widths for SNe Ia [though Sim et al. (2013) do not recover the observed WLR].

Another popular scenario for SN Ia progenitor systems is the double-degenerate (DD; Tutukov & Iungelson 1976; Tutukov & Yungelson 1979; Iben & Tutukov 1984; Webbink 1984) scenario in which two WDs in a close binary merge after orbital decay due to gravitational radiation. Some recent simulation results have shown that a violent merger of the two WDs produces 'hotspots' which exceed the critical temperature and density (Seitenzahl et al. 2009b) needed to ignite CO fusion (Guillochon et al. 2010; Lorén-Aguilar, Isern & García-Berro 2010; Pakmor et al. 2010, 2013; Moll et al. 2014; Raskin et al. 2014). This scenario is inherently not tied to $M_{\rm Ch}$, but instead could produce explosions with varying luminosities and light-curve widths simply due to the variation in mass of the progenitor system (Ruiter et al. 2013). Generally for the DD scenario, the WD undergoes a complete detonation and the amount of ^{56}Ni produced depends on the mass of the progenitor (Fink et al. 2010; Sim et al. 2010).

Finally, it is important to also consider the double-detonation (DDet) mechanism for triggering the WD explosion. In this scenario, helium-rich material accreted on to the surface of the WD (either from an He-rich main-sequence or giant star or He-WD) could ignite and send a shockwave into the core of the star. This shock wave then triggers a second detonation near the WD core which initiates the thermonuclear runaway process (Livne 1990; Iben & Tutukov 1991; Woosley & Weaver 1994; Fink et al. 2010; Woosley & Kasen 2011; Shen & Moore 2014). This mechanism could arise from SD or DD systems, and is not tied to $M_{\rm Ch}$. Additionally, this mechanism may offer a favourable explanation for the presence of high-velocity features in early SN Ia spectra (Mazzali et al. 2005; Maguire et al. 2012, 2014; Childress et al. 2013a, 2014b; Marion et al. 2013; Pan et al. 2015a; Silverman et al. 2015).

While much of the debate about SN Ia progenitors in the previous decade revolved around which single scenario was responsible for SNe Ia, recent results have pointed towards multiple progenitor channels being realized in nature. SN Ia rates studies yielded evidence for both short- and long-lived progenitors (Mannucci et al. 2005; Scannapieco & Bildsten 2005; Mannucci, Della Valle & Panagia 2006; Sullivan et al. 2006; Aubourg et al. 2008). The lack of a detected companion star to the progenitor of SN 2011fe (Li et al. 2011) and in SN Ia remnants (e.g. Kerzendorf et al. 2012, 2013, 2014a; Schaefer & Pagnotta 2012) presents individual cases where the DD scenario seems necessary, while strong emission from circumstellar material in some nearby SNe Ia (Hamuy et al. 2003; Aldering et al. 2006; Dilday et al. 2012; Silverman et al. 2013a,c) seems to indicate clear cases of the SD scenario. Other progenitor scenarios beyond SD and DD are also currently under consideration by the SN Ia community, such as the core-degenerate scenario (see, e.g., Tsebrenko & Soker 2015).

For peculiar WD SNe, like the Type Iax SN 2012Z, a luminous progenitor system has been detected and interpreted as the donor star (McCully et al. 2014a). Recently, shock interaction of SN ejecta with a (non-degenerate) companion star has been detected in the early light curve of another peculiar, low-velocity WD SN (Cao et al. 2015). Similarly, the first evidence for such shock interaction in a normal SN Ia has been observed for SN 2012cg (Marion et al. 2015). However, such shock interaction is distinctly absent for several other SNe Ia observed continuously through the epoch of first light with the *Kepler* satellite (Olling et al. 2015). Additionally, a general dichotomy in many of the spectroscopic properties of SNe Ia appears evident (e.g. Wang et al. 2009b, 2013; Maguire et al. 2014). Thus, numerous lines of evidence now point to multiple SN Ia progenitor channels being active.

Variations in progenitor masses between different explosion mechanisms will manifest as diversity in the bolometric light curves of SNe Ia (Arnett 1982; Jeffery 1999; Stritzinger et al. 2006a; Röpke et al. 2012). Recently, Scalzo et al. (2014a) demonstrated that the ejected mass – hence the progenitor mass – of an SN Ia could be recovered to 10–15 per cent precision, as tested on bolometric light curves derived from radiative transfer modelling of SN Ia explosion models with known input progenitor mass. Applying the same modelling technique to real data, Scalzo et al. (2014a) found evidence that the ejected mass varies in the range 0.9–1.4 M$_\odot$ among spectroscopically normal (Branch, Fisher & Nugent 1993) SNe Ia and that the ejected mass also correlates strongly with the light-curve width parameter used to standardize SN Ia distances in cosmology. The correlation between ejected mass and light-curve width was exploited by Scalzo, Ruiter & Sim (2014b) to measure the SN Ia ejected mass distribution: they found that 25–50 per cent of all normal SNe Ia eject sub-Chandrasekhar (sub-Ch) masses, with most of the rest being consistent with Chandrasekhar-mass events. This is consistent with constraints from Galactic chemical evolution based on Mn/Fe in the solar neighbourhood (Seitenzahl et al. 2013b) which require some non-negligible contribution from Chandrasekhar-mass SNe Ia. Similarly, Yamaguchi et al. (2015) placed tight constraints on the progenitor mass of the SN remnant 3C 397, finding that it must have originated from a Chandrasekhar-mass progenitor. Scalzo et al. (2014b) found that super-Chandrasekhar-mass SNe Ia were very rare, at most a few per cent of all SNe Ia, consistent with previous measurements of the relative rate (Scalzo et al. 2012).

The diversity in ejected mass suggests a corresponding diversity in explosion mechanisms among normal SNe Ia. Further information about the explosion mechanism may also be encoded in the peak absolute magnitude distribution (Ruiter et al. 2013; Piro,

Thompson & Kochanek 2014), the diversity in early SN Ia light curves (Dessart et al. 2014c), or in the relation between ^{56}Ni and ejected mass (Sim et al. 2010; Ruiter et al. 2013; Scalzo et al. 2014a). The ^{56}Ni mass is most commonly inferred from the peak absolute magnitude of the SN (Arnett 1982), although with some model-dependent systematic errors (Branch 1992; Hoeflich & Khokhlov 1996; Howell et al. 2009). The ^{56}Ni mass can also be inferred from detailed modelling of photospheric phase spectral times series (Stehle et al. 2005; Mazzali et al. 2008; Tanaka et al. 2011; Sasdelli et al. 2014; Blondin, Dessart & Hillier 2015) or modelling nebular spectra (e.g. Mazzali et al. 2011, 2015; Mazzali & Hachinger 2012). Reliable alternative methods for measuring ^{56}Ni masses, with different model-dependent systematics, can thus in principle help to shed light on the explosion mechanisms and progenitor properties of SNe Ia.

In this work, we show that the amount of ^{56}Ni produced in the SN Ia explosion can be measured directly from signatures of its decay product ^{56}Co in nebular phase spectra of SNe Ia. Specifically, we employ the flux of the [Co III] $\lambda5893$ line in spectra of SNe Ia in the nebular phase ($t \geq 150$ d past maximum brightness) as a diagnostic of the mass of ^{56}Co at a given epoch. Kuchner et al. (1994) showed that the ratio of the flux of this line to the Fe III line at $\lambda4700$ Å as a function of SN phase followed the expected temporal evolution of the Co/Fe mass ratio, which they used as evidence for the presence of ^{56}Ni generated in the SN explosion. More recently, the presence of ^{56}Ni has been directly confirmed through gamma-ray line emission from the ^{56}Ni (Diehl et al. 2014) and ^{56}Co (Churazov et al. 2014) lines observed by the *INTEGRAL* satellite for the very nearby SN 2014J.

Previous studies of SN Ia nebular spectra have collected a modest sample of spectra (a few dozen) from which important scientific results were derived. Mazzali et al. (1998) found a strong correlation between the width of nebular emission lines (specifically the Fe III 4700 feature) with the SN light-curve stretch, constituting evidence for greater ^{56}Ni production in more luminous slow-declining SNe Ia. This result was combined with detailed modelling of nebular spectra (especially the 7380 Å nebular line presumed to arise from stable ^{58}Ni) to infer a common explosion mechanism for SNe Ia (Mazzali et al. 2007). Nebular spectra have also been employed to place upper limits on hydrogen in the vicinity of normal SNe Ia (Leonard 2007; Shappee et al. 2013; Graham et al. 2015b; Lundqvist et al. 2015). The lack of hydrogen in normal SNe Ia is in contrast to the strong hydrogen lines found in late-phase spectra of SNe Ia which exhibited strong interaction during the photospheric phase (Silverman et al. 2013a). Velocity shifts in the purported Ni 7380 Å nebular line were used to infer asymmetry in the inner core of SNe Ia (Maeda et al. 2010a,b), which was also found to correlate with the optical colour and Si 6355 Å velocity gradient during the photospheric phase (Maeda et al. 2011). These line velocity shifts were found to also correlate with photospheric phase spectropolarimetry (Maund et al. 2010), indicating a general correlated asymmetric geometry for SNe Ia. These early results have generally been supported with greater statistics afforded by new large data sets such as the CfA sample (Blondin et al. 2012) and BSNIP (Silverman, Ganeshalingam & Filippenko 2013b, though these works found a weaker correlation of SN stretch with the Fe III 4700 line width).

Until recently, the nebular line at 5893 Å was not frequently emphasized as a diagnostic of ^{56}Co due to its presumed association with emission from sodium (Kuchner et al. 1994; McClelland et al. 2013 are noteworthy exceptions). However, Dessart et al. (2014a) showed definitively that this line arises primarily from cobalt for the majority of SNe Ia. Inspired by this result, we use the [Co III]

$\lambda5893$ line as a diagnostic of ^{56}Ni from a large sample of nebular SN Ia spectra compiled from both new observations and from the literature. Equipped with a sample of SN Ia spectra from the literature and new spectra from our own observations, we calculate the *absolute* flux of the nebular [Co III] $\lambda5893$ line by scaling the spectra to flux-calibrated photometry measurements. With these calibrated fluxes, we show that the temporal evolution of the absolute [Co III] $\lambda5893$ line flux (specifically, the slope of logarithmic flux versus time) is highly consistent across all SNe Ia with multiple nebular spectra. We exploit this result to place measurements from disparate epochs on a common scale. This allows us to meaningfully compare the line fluxes in order to determine the relative amount of ^{56}Ni produced by each SN Ia in our sample.

In Section 2 we present our compilation of literature SN Ia spectra and the new nebular SN Ia data released here. Section 3 presents our method for measuring the [Co III] $\lambda5893$ flux from the spectra and scaling the spectra with the SN Ia photometry. We examine the temporal evolution of the [Co III] $\lambda5893$ for SNe Ia with numerous nebular observations in Section 4. We then infer ^{56}Ni masses for our SN Ia sample in Section 5, and discuss the implications and limitations of our results in Section 6. Finally, we conclude in Section 7.

2 SN IA NEBULAR SPECTROSCOPY DATA

The analysis in this work relies on a compilation of SN Ia nebular spectra from the literature as well as new observations. The full sample of literature and new late-phase spectra are presented in Table 1. Host galaxy redshifts and distances used later in the analysis can be found in Appendix B in Table B1. Photospheric phase light-curve information and their sources are listed in Table B2.

2.1 Compilation of literature data

For reasons outlined in Section 4, the earliest epochs from which we can use [Co III] $\lambda5893$ line fluxes are at phase $t = +150$ d. In practice, we found for most spectra beyond $t \approx +400$ d that the [Co III] $\lambda5893$ flux was too weak to be usable for our preferred analysis. Furthermore, Taubenberger et al. (2015) recently showed that the $t = +1000$ d spectrum of SN 2011fe showed dramatic changes in its structure, likely arising from a change in the ionization condition of the nebula. Indeed, this ionization change appears evident in the $t = +590$ d spectrum presented in Graham et al. (2015b), and we see evidence for the onset of this change shortly after $t \approx +400$ d in the data gathered for this analysis. Thus, we excise data later than $t \approx +400$ d as unreliable due to low signal and likely ionization change (we examine potential impact from the latter effect in Section 6.2).

To begin compiling a sample that meets these phase criteria, we performed a large query of the Weizmann Interactive Supernova data REPository (WISeREP[1] – Yaron & Gal-Yam 2012) data base to search for SNe Ia with two spectroscopic observations separated by at least 100 d – assuming that the earlier one would be near maximum light, this singles out SNe Ia with nebular spectra. We then require SNe to have photospheric phase optical light curves sufficient to robustly establish light-curve stretch, colour, and the date of maximum light using SiFTO (Conley et al. 2008). We also require the spectra to have sufficiently high signal-to-noise (S/N) so that the [Co III] $\lambda5893$ line can be well fitted using a Gaussian fitting procedure (see Section 3). SN 2006X was excluded (despite

---

[1] http://wiserep.weizmann.ac.il

Table 1. New and literature late-phase SN Ia spectra.

SN	Phase t^a (d)	Obs. date^b	Spec. ref.^{c}
SN 1990N	160	19901217	BSNIP
	186	19910112	Gómez & López (1998)
	227	19910222	Gómez & López (1998)
	255	19910322	Gómez & López (1998)
	280	19910416	Gómez & López (1998)
	333	19910608	Gómez & López (1998)
SN 1991T	186	19911031	BSNIP
	258	19920111	Gómez & López (1998)
	320	19920313	BSNIP
	349	19920411	BSNIP
SN 1994ae	144	19950422	BSNIP
	153	19950501	CfA
SN 1995D	277	19951124	CfA
	285	19951202	CfA
SN 1998aq	211	19981124	Branch et al. (2003)
	231	19981214	Branch et al. (2003)
	241	19981224	Branch et al. (2003)
SN 1998bu	179	19981114	CfA
	190	19981125	CfA
	208	19981213	CfA
	217	19981222	CfA
	236	19990110	BSNIP
	243	19990117	CfA
	280	19990223	BSNIP
	329	19990413	Cappellaro et al. (2001)
	340	19990424	BSNIP
SN 1999aa	256	19991109	BSNIP
	282	19991205	BSNIP
SN 2002cs	174	20021106	BSNIP
SN 2002dj	222	20030201	Pignata et al. (2008)
	275	20030326	Pignata et al. (2008)
SN 2002er	216	20030410	Kotak et al. (2005)
SN 2002fk	150	20030227	BSNIP
SN 2003du	109	*20030823*	Stanishev et al. (2007)
	138	*20030921*	Anupama, Sahu & Jose (2005)
	139	*20030922*	Anupama et al. (2005)
	142	*20030925*	Stanishev et al. (2007)
	209	20031201	Stanishev et al. (2007)
	221	20031213	Stanishev et al. (2007)
	272	20040202	Stanishev et al. (2007)
	377	20040517	Stanishev et al. (2007)
SN 2003hv	113	*20031228*	Leloudas et al. (2009)
	145	*20040129*	Leloudas et al. (2009)
	323	20040725	Leloudas et al. (2009)
SN 2004bv	171	20041114	BSNIP
SN 2004eo	228	20050516	Pastorello et al. (2007)
SN 2005cf	319	20060427	Wang et al. (2009a)
SN 2007af	103	*20070620*	CfA
	108	*20070625*	CfA
	120	*20070707*	BSNIP
	123	*20070710*	CfA
	128	*20070715*	BSNIP
	131	*20070718*	CfA
	151	20070807	BSNIP
	165	20070821	BSNIP
	308	20080111	CfA
SN 2007gi	161	20080115	Zhang et al. (2010)
SN 2007le	317	20080827	BSNIP
SN 2007sr	177	20080623	CfA
SN 2009le	324	20101016	T15b
SN 2011by	206	20111202	Silverman et al. (2013b)

Table 1. – *continued.*

SN	Phase t^a (d)	Obs. date^b	Spec. ref.^{c}
	310	20120315	Silverman et al. (2013b)
SN 2011fe	74	*20111123*	Shappee et al. (2013)
	114	*20120102*	Shappee et al. (2013)
	196	20120324	Shappee et al. (2013)
	230	20120427	Shappee et al. (2013)
	276	20120612	Shappee et al. (2013)
	314	20120720	Taubenberger et al. (2015)
SN 2011iv	318	20121024	T15b
SN 2012cg	330	20130507	M15
	342	20130513	T15b
SN 2012fr	51	*20130102*	This work
	62	*20130113*	This work
	77	*20130128*	This work
	101	*20130221*	This work
	116	*20130308*	This work
	125	*20130317*	This work
	151	20130412	This work
	222	20130622	This work
	261	20130731	This work
	340	20131018	This work
	357	20131103	M15
	367	20131114	This work
SN 2012hr	283	20131006	This work
SN 2013aa	137	*20130710*	This work
	185	20130827	This work
	202	20130913	This work
	342	20140131	This work
	358	20140216	M15
SN 2013cs	322	20140324	M15
SN 2013dy	333	20140626	Pan et al. (2015a)
SN 2013gy	276	20140920	This work
SN 2014J	231	20140920	This work

Notes. ^{a}Observer frame phase with respect to date of *B*-band peak brightness.
^{b}Observation dates that are *italicized* are not used to measure M_{Ni}, and are only employed in Section 4.
^{c}BSNIP: Silverman et al. (2012a); CfA: Matheson et al. (2008); Blondin et al. (2012); M15: Maguire et al. (in preparation); T15b: Taubenberger et al. (in preparation).

having numerous nebular spectra) due to significant variability in its sodium features (Patat et al. 2007) and a rather significant light echo (Crotts & Yourdon 2008; Wang et al. 2008), both of which might affect the time evolution of the [Co III] λ5893 flux.

Finally, we excise any SNe Ia which are spectroscopically peculiar in the nebular phase: SNe Ia similar to SN 1991bg (Filippenko et al. 1992a; Leibundgut et al. 1993) exhibit extremely narrow Fe lines and unusual line ratios; Ia-CSM SNe (Silverman et al. 2013a) are excluded due to possible impact of circum-stellar material (CSM) on the nebular emission; SNe Iax (Foley et al. 2013) are excised as these probably arise from a different physical mechanism than normal SNe Ia; candidate super-Chandrasekhar SNe Ia (Howell et al. 2006) are excised due to their unusual nebular spectra (Taubenberger et al. 2013). SNe Ia similar to SN 1991T (Filippenko et al. 1992b; Phillips et al. 1992) or SN 1999aa *are* however included in the sample, as their ionization structure appears to be similar to 'normal' SNe Ia.

In summary, the selection criteria for our sample of literature nebular SN Ia spectra are

(i) phase (with respect to *B*-band maximum light) in the range $+150 \leq t \leq +400$,

Table 2. Observation details for new late-phase SN Ia spectra.

SN	Phase [a] (d)	Obs. date	Telescope/instrument
SN 2012fr	+51	2013-Jan-02	NTT-3.6 m/EFOSC
	+62	2013-Jan-13	NTT-3.6 m/EFOSC
	+77	2013-Jan-28	NTT-3.6 m/EFOSC
	+101	2013-Feb-21	NTT-3.6 m/EFOSC
	+116	2013-Mar-08	ANU-2.3 m/WiFeS
	+125	2013-Mar-17	NTT-3.6 m/EFOSC
	+151	2013-Apr-12	ANU-2.3 m/WiFeS
	+222	2013-Jun-22	ANU-2.3 m/WiFeS
	+261	2013-Jul-31	ANU-2.3 m/WiFeS
	+340	2013-Oct-18	SALT/RSS
	+367	2013-Nov-14	ANU-2.3 m/WiFeS
SN 2012hr	+283	2013-Oct-06	Gemini/GMOS
	+368	2013-Dec-30	ANU-2.3 m/WiFeS
SN 2013aa	+137	2013-Jul-10	SALT/RSS
	+185	2013-Aug-27	SALT/RSS
	+202	2013-Sep-13	ANU-2.3 m/WiFeS
	+342	2014-Jan-31	ANU-2.3 m/WiFeS
SN 2013cs	+320	2014-Mar-22	ANU-2.3 m/WiFeS
SN 2013dy	+419	2014-Sep-20	Keck-II/DEIMOS
SN 2013gy	+276	2014-Sep-20	Keck-II/DEIMOS
SN 2014J	+231	2014-Sep-20	Keck-II/DEIMOS

Notes. [a]Observer frame phase with respect to date of *B*-band peak brightness.

(ii) well-sampled multi-colour photospheric phase light curve (such that the light-curve fitter SiFTO converges),

(iii) sufficient spectrum S/N to measure the [Co III] λ5893 line centre and width, and

(iv) no spectroscopic peculiarity, except SN 1991T-like.

The full sample of spectra which meet these criteria are presented in Table 1, and comprise 54 spectra of 23 SNe Ia from the literature. Table 1 also lists 14 literature spectra of 4 SNe Ia from phases earlier than $t = +150$ d which are employed in the analysis of gamma-ray trapping in Section 4.3.

Finally, we note that two of the SNe in our sample had prominent light echoes at late times: SN 1991T (Schmidt et al. 1994) and SN 1998bu (Spyromilio et al. 2004). For both of these SNe, the light echo contributions are negligible at the spectroscopic epochs we employ.

2.2 New SN Ia nebular spectroscopy

We obtained new late-phase ($+50 \leq t \leq +150$ d) and nebular ($t \geq +150$ d) spectra of several nearby SNe Ia from numerous telescopes. These spectra have been released publicly on WISeREP, with several spectra of SN 2012fr released through ESO data releases for the Public ESO Spectroscopic Survey for Transient Objects (PESSTO[2] – Smartt et al. 2015). Observation details are presented in Table 2 and a plot of the spectra is shown in Fig. 1. We note that these spectra have not been rescaled to match observed photometry.

Several late-phase spectra of very nearby SNe Ia were collected with the Wide Field Spectrograph (WiFeS; Dopita et al. 2007, 2010) on the Australian National University (ANU) 2.3 m telescope at Siding Spring Observatory in northern New South Wales, Australia. Observations were performed with the B3000 and R3000 gratings with the RT560 dichroic, giving wavelength range of 3500–9800 Å, with resolution of 0.8 and 1.2 Å on the blue and red arms, respectively. Data were reduced using the PYWIFES package (Childress et al.

2014a), and spectra were extracted using our custom GUI (see e.g. Childress et al. 2013a). We generally observed during very dark nights (moon illumination less than 20 per cent) when the seeing was favourable (1.5–2.0 arcsec). We note that the WiFeS spectra of SN 2012hr and SN 2013cs have too low S/N to obtain a reliable measurement of the [Co III] λ5893 line flux, but we release them publicly (on WISeREP) here.

New nebular spectra for three nearby SNe Ia were collected with DEIMOS (Faber et al. 2003) on the Keck-II telescope on Mauna Kea, Hawaii. Observations were conducted with a 1.5 arcsec longslit, the 600 l/mm grating with a central wavelength of 5000 Å and with the GG410 order blocking filter, yielding a wavelength range of 4000–7650 Å with 0.6 Å resolution. Data were reduced using standard techniques in IRAF (see e.g. Childress et al. 2013b), with the blue and red chips reduced separately and then combined as a final step. We employed the Mauna Kea extinction curve of Buton et al. (2013). Our observations come from a single night on Keck (2014-Sep-20 UTC) when conditions were less favourable (high humidity and thick clouds, ultimately 50 per cent time lost to weather) but with a median seeing of 0.9 arcsec.

Five additional late-phase spectra of SN 2012fr were collected as part of the PESSTO during early 2013, and reduced with the PESSTO pipeline as described in Smartt et al. (2015). One spectrum of SN 2012fr and two spectra of SN 2013aa were obtained in 2013 using the Robert Stobie Spectrograph (Nordsieck et al. 2001) on the South African Large Telescope (SALT), and reduced using a custom pipeline that incorporates PYRAF and PYSALT (Crawford et al. 2010). One spectrum of SN 2012hr was obtained with Gemini GMOS (Hook et al. 2004) using the 0.75 arcsec longslit with the B600 and R400 gratings in sequence to yield a spectral coverage from 4000–9600 Å, under programme GS-2013B-Q-48 (PI: Graham) – the spectrum was reduced using the Gemini IRAF package.

In the analysis below, we also include nebular spectroscopy samples from forthcoming analyses by Maguire et al. (in preparation – hereafter M15) and Taubenberger et al. (in preparation – hereafter T15b). The M15 sample were obtained over a multi-period programme at the VLT using XShooter (Vernet et al. 2011), and were reduced with the XShooter pipeline (Modigliani et al. 2010) using standard procedures (as in Maguire et al. 2013). The T15b sample were observed as part of a separate multi-period programme using FORS2 on the VLT, and data were reduced with standard procedures similar to those employed in Taubenberger et al. (2013). Where possible, the T15b and M15 spectra were flux calibrated with contemporaneous photometry taken with the VLT; in other instances, literature photometry was employed (see Appendix B for details).

In total, we release 21 new spectra of 7 SNe Ia on WISeREP: 11 spectra of 5 SNe Ia used to derive ^{56}Ni masses, 7 early ($t \leq 150$ d) spectra of 2 SNe Ia used to inspect gamma-ray trapping, and 3 spectra of 3 SNe Ia which are too late or have too low S/N for our analysis. We also employ seven spectra of six SNe Ia from M15 and T15b.

3 NEBULAR LINE FLUX MEASUREMENTS

3.1 The [Co III] λ5893 line in the nebular phase: a radiative transfer perspective

The current study was motivated by the disappearance of Co III lines in the nebular time series spectra analysed here, most notably the [Co III] λ5893 feature. Previous literature analyses have attributed
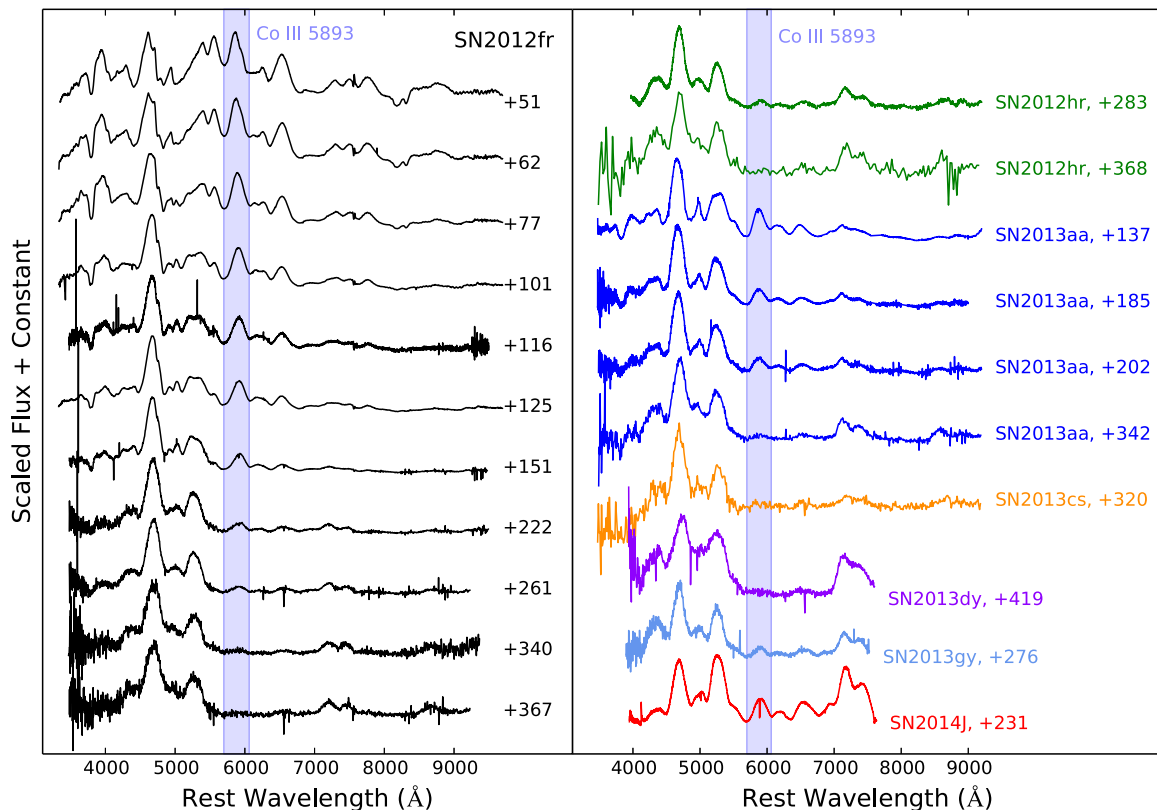
Figure 1. New late-phase and nebular spectra of SNe Ia presented in this work, labelled by phase with respect to the epoch of *B*-band peak brightness. All spectra are publicly available on WISeREP. Some spectra have been slightly binned (to ~5 Å) for visual clarity.

this feature alternately to Co III and Na I, so we turned to radiative transfer calculations to settle this ambiguity.

We employed the time-dependent radiative transfer code CMFGEN (Hillier & Dessart 2012), which solves the time-dependent radiative transfer equation simultaneously with the kinetic equations. Given an initial explosion model, we self-consistently solve for the temperature structure, the ionization structure, and the non-local thermodynamic equilibrium populations, beginning the calculations at 0.5–1 d after the explosion. The modelling assumes homologous expansion, typically uses a 10 per cent time step, and no changes are made to the ejecta structure (other than that required by homologous expansion) as the ejecta evolve in time. Further details about the general model set up, and model atoms, can be found in Dessart et al. (2014c). We deployed CMFGEN on a delayed-detonation model (DDC10 – Blondin et al. 2013; Dessart et al. 2014c) at very late phases and examine the contribution of various ions to the nebular emission spectrum. Radiative transfer calculations for this model, and similar models but with a different initial ^{56}Ni mass, have shown favourable agreement with observations (Blondin et al. 2013, 2015; Dessart et al. 2014a,b,c).

In Fig. 2, we show DDC10 modelled with CMFGEN at phases +126 d (left-hand panels) and +300 d (right-hand panels). The top panels in each column show the integrated DDC10 model flux compared to observations of nebular phase SNe Ia at similar phases, while the bottom panels show the line emission from individual ions (note that this can exceed the integrated flux due to the net opacity encountered by photons following their initial emission). The +126 d model shows particularly good agreement with the data. At +300 d, the model shows some discrepancy with the data, particularly in the ionization state of the nebula.

Most importantly, the radiative transfer calculations show that the emission feature near 5900 Å is clearly dominated by Co III emission, with little or no contamination from other species. Few other features in the optical region of the spectrum show such clean association with a single ion.

For later aspects of our analysis, we require the velocity centre of the nebula, which we calculate from the [Co III] λ5893 line. To do so requires an accurate calculation of the mean rest wavelength for this line complex. The [Co III] λ5893 arises from the 3d^7 a^{4}F– 3d^7 a^{2}G multiplet, and is actually a blend of two lines – one at 5888.5 Å and a second, but weaker, line at 5906.8 Å (see Appendix A and Table A1). Given the *A* values and wavelengths of the transitions contributing to the line complex, the weighted mean rest wavelength of the Co III line is 5892.7 Å (note that this and previous are air wavelengths). Henceforth, we use this value for calculating line velocities.

3.2 Measuring the [Co III] λ5893 line flux

For the main analyses in this work, we focus on the flux in the [Co III] λ5893 line. We measure the flux in this line as follows.

We perform an initial Gaussian fit to the [Co III] λ5893 line in order to determine the centre and width of the line (note that because the spectrum is pure emission at these late phases we assume a continuum level of zero). We then integrate the flux within ±1.5σ of the fitted line centre and use this 'integral' flux for the remainder of this paper. This integral boundary was chosen as a compromise between capturing a large fraction of the emitted line flux (97 per cent for a strictly Gaussian profile) and limiting contamination from neighbouring emission lines. Generally, the integrated line flux and that calculated from the best Gaussian fit showed excellent agreement
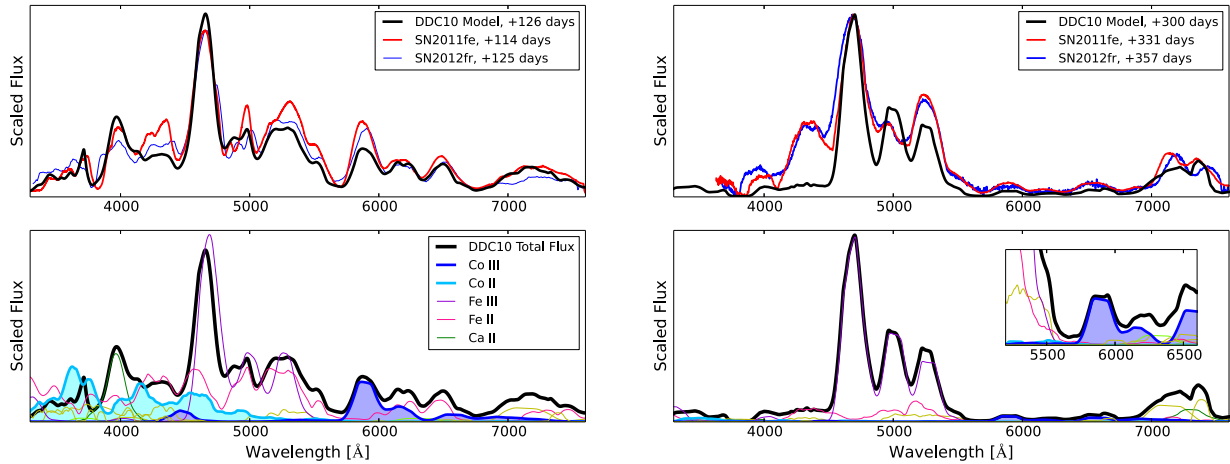
Figure 2. Top panels: comparison of radiative transfer (CMFGEN) model spectrum for the DDC10 (Blondin et al. 2013) delayed-detonation model at very late epochs (left: +126 d, right: +300 d) compared to contemporaneous data for SN 2011fe and SN 2012fr. Bottom panels: emission spectra for various ions from CMFGEN for late-phase DDC10 models (epochs as above).
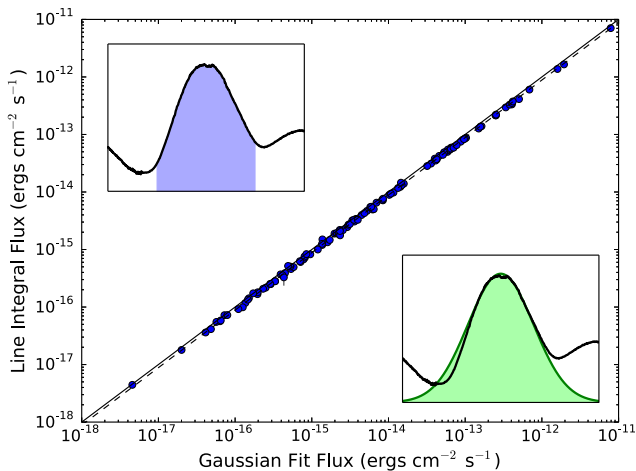

Figure 3. Comparison of flux in the [Co III] λ5893 line measured in two ways: strict integration of the spectrum flux within $\pm 1.5\sigma$ of the fitted line centre (*y*-axis and upper-left inset) and the formal integral of the best-fitting Gaussian profile (*x*-axis and lower-right inset). The solid line represents unity, while the dashed line is the mean ratio of the integral flux to Gaussian flux for the full sample (0.88 ± 0.05, median ratio is 0.87). Measurement error bars are shown but are generally smaller than the data points.

(see Fig. 3), but we prefer the integral flux as this is robust against non-Gaussianity of the line profile.

For SNe Ia with multiple nebular spectra, we enforce common wavelength bounds for the flux integration at all epochs, as determined by the median fitted line centre and width values across all epochs. This is because at these late epochs the nebula is optically thin (in contrast to the optically thick earlier epochs; see Taubenberger et al. 2009, for an example with nebular core-collapse SN spectra). Thus, at these epochs the line profile reflects the true physical extent of the emitting species (in velocity space). We also verified that the fitted line centres for the [Co III] λ5893 feature did not evolve in time after phases +150 d, validating our approach.

To place our [Co III] λ5893 line flux measurements on the correct absolute scale, we must ensure that the spectra have the correct *absolute* flux calibration. To achieve this, we measure the expected *B*-band flux in the spectrum by convolving it with the *B*-band filter throughput curve and integrating. We then compute the ratio of this flux collected in the spectrum *B* passband to the true *B*-band flux of the SN at that epoch. The latter is determined from the late-time photometry for each of our SNe, as outlined in Appendix B and presented in Table B3. To ensure reproducibility of our results, we report in this table the flux values derived from the raw measurements made from the spectra in their published form.

We note that normalization with the *B* band could introduce errors in the [Co III] λ5893 flux due to chromatic errors in the spectrum's flux calibration. However, previous authors consistently performed chromatic flux calibration using spectrophotometric standard stars, typically yielding excellent colour agreement with observed photometry (e.g. $B - V$ scatter of 0.08 mag and 0.10 mag for the CfA and BSNIP samples, respectively). We also note that other systematic effects could affect our measurements of [Co III] λ5893 line flux. These include contamination from neighbouring nebular emission lines (e.g. Fe II lines, see Fig. 2), residual host galaxy light, or perhaps even previously undetected light echoes (see, e.g., Spyromilio et al. 2004). Thus, we expect a conservative estimate for the systematic uncertainty in the [Co III] λ5893 flux measurement to be about 10 per cent of the measured flux.

The final integrated [Co III] λ5893 line flux, wavelength bounds for the integral, and scale factor applied to the spectrum to match synthetic *B*-band flux (integrated from the spectrum) to the observe *B*-band magnitude are all presented in Table B4. Variance spectra were not available for many of the literature SN Ia spectra in our analysis. To correct this, we smooth the spectrum with a Savitzky–Golay filter (Savitzky & Golay 1964), then smooth the squared residuals of the data from this smooth curve to derive a variance spectrum measured directly from the noise in the data (as we did for data in Childress et al. 2014b). [Co III] λ5893 line flux measurement errors were then determined from these corrected variance spectra, and these measurement errors are the values reported in the table.

4 EVOLUTION OF THE [CO III] λ5893 LINE FLUX

4.1 Theoretical expectations for [Co III] λ5893 evolution

The decay of ^{56}Co to ^{56}Fe produces positrons and energetic gamma-rays. The charged positrons carry kinetic energy which they lose

to the surrounding medium via Coulomb interactions. At the nebular densities present at late times, the length-scale for positron energy deposition is much smaller than the size of the nebula so the positrons essentially deposit all of their kinetic energy locally (Chan & Lingenfelter 1993). gamma-rays – either those emitted directly from ^{56}Co decay or created when the positrons annihilate – are subject to radiative transfer effects and will eventually free stream as the SN nebula expands and decreases its density enough to become optically thin to gamma-rays. The onset of this phase – where positrons deposit a constant fraction of energy into the SN nebula and gamma-rays escape fully – has been observed in late SN Ia bolometric light curves (e.g. Sollerman et al. 2004; Stritzinger & Sollerman 2007; Leloudas et al. 2009; Kerzendorf et al. 2014b).

Our expectation from a simple energetics perspective is that the flux of the [Co III] λ5893 line should evolve as the square of the mass of cobalt as a function of time $M_{Co}(t)$, and our argument is as follows. The energy being deposited into the nebula at these late phases arises from the positrons produced in ^{56}Co decay, and thus should scale with the mass of cobalt. If this energy is evenly deposited amongst all species in the nebula, then the fraction of that energy absorbed by the cobalt atoms should be proportional to the mass fraction of cobalt. Thus, the amount of energy absorbed by cobalt atoms follows the square of the cobalt mass as a function of time. If the fraction of that energy emitted in the [Co III] λ5893 line remains constant (see Section 6.2), then we expect a net quadratic dependence of the [Co III] λ5893 line luminosity on the mass of cobalt as a function of time.

Observational evidence for this temporal evolution of the [Co III] λ5893 line should be expected from prior results. The late-phase bolometric light curves of SNe Ia closely follow the amount of energy deposited by the decay of ^{56}Co (see, e.g., Sollerman et al. 2004). It was also demonstrated by Kuchner et al. (1994) that the ratio of [Co III] λ5893 to Fe 4700 emission follows the Co/Fe mass ratio (as noted above), and the Fe 4700 line flux generally scales with the total luminosity of the SN since Fe is the primary coolant. These facts combine to lend an expectation that the net emission from the [Co III] λ5893 line should scale quadratically with the mass of Co in the SN nebula as a function of time. Indeed, McClelland et al. (2013) found such a quadratic dependence for the [Co III] λ5893 line in SN 2011fe.

The above reasoning for M_{Co}^2 dependence of the [Co III] λ5893 flux holds for epochs when the nebula is fully transparent to gamma-rays. Thus, it is important to inspect the theoretical expectation for the timing of this gamma-ray transparency in the IGE zone. The energy released per decay from ^{56}Co is 3.525 MeV, of which 3.3 per cent is associated with the kinetic energy of the positrons (Huo, Huo & Dong 2011), and we have ignored the energy associated with neutrinos. As the expansion is homologous, the optical depth associated with gamma-rays scales as $1/t^2$. Assuming that the kinetic energy of the positrons is captured locally, the energy absorbed per ^{56}Co decay in MeV is

$$e_{Co} = 0.116 + 3.409 \left(1 - \exp[-\tau_o(t_o/t)^2]\right),$$ (1)

where τ_o is the effective optical depth at a time t_o. If we denote t_c as the time at which energy deposition by gamma-rays and positrons are equal [i.e. when the two terms from equation (1) are equal], then equation (1) can be rewritten as

$$E_{Co} \propto M_{Co} \left(1 - 0.967 \exp\left[-0.0346(t_c/t)^2\right]\right).$$ (2)

We expect that the flux from the [Co III] λ5893 line would further scale as

$$F_{Co} \propto E_{Co} \times \frac{x M_{Co}/M_{IGE}}{1 + (a-1)M_{Co}/M_{IGE} + b M_{Ot}/M_{IGE}},$$ (3)

where M_{IGE} is the total mass of the IGE zone, a and b are respectively the (time-dependent) factors relating the cooling efficiency of Co and other species (which have total mass of M_{Ot}) relative to iron, and x is the factor scaling the emission in the [Co III] λ5893 feature. If the thermal conditions in the SN nebula are relatively stable (i.e. constant x) and cooling by non-iron species is negligible (i.e. the above denominator goes to unity), then the line flux simply becomes proportional to M_{Co}/M_{IGE}. Combining equations (2) and (3) yields

$$F_{Co} \propto M_{Co}^2 \left(1 - 0.967 \exp\left[-0.0346(t_c/t)^2\right]\right).$$ (4)

For the DDC10 model, we find $t_c \sim 214$ d (from explosion) – this would imply a deviation from M_{Co}^2 of a factor of 2 from +150 to +400 d (assuming a rise time of ~17 d), or a factor of 1.5 from +200 to +400 d. Alternatively, if $t_c \sim 80$ d (see Section 4.3), then the deviation from M_{Co}^2 is only 20 per cent from +150 to +400 d and 10 per cent from +200 to +400 d.

4.2 Observed [Co III] λ5893 evolution in nebular spectral time series

To examine the observed evolution of the [Co III] λ5893 line, we turn to those SNe Ia with numerous nebular spectra. Specifically, we isolate the subset of SNe Ia in our sample with at least three epochs of observation later than +150 d past maximum. For the eight SNe Ia in our sample which meet this criterion, we also collect spectra within $+100 \leq t \leq +150$ d past maximum (dates listed in italics in Table 1). These additional spectra allow us to further inspect the [Co III] λ5893 flux evolution, but these spectra are not employed in our nickel mass estimates derived in Section 5.

In the left-hand panel of Fig. 4, we show the evolution of the [Co III] λ5893 line luminosity versus time for our sample of SNe Ia with three or more observations after +150 d. We plot the line evolution for a linear (dotted) line and quadratic (solid line) dependence on $M_{Co}(t)$, with both curves normalized at phase $t = +200$ d. For each SN in this subset, we fit for a single multiplicative scaling factor that minimizes the residuals of the $M_{Co}(t)^2$ line (i.e. we normalize each SN data set to that line – thus the reason for requiring multiple data points per SN). This isolates the time dependence of the line flux (which depends on the SN nebula physics) by removing its absolute magnitude (which depends on the quantity of ^{56}Ni produced).

The evolution of the [Co III] λ5893 line shows remarkable agreement with the expected trend of $M_{Co}(t)^2$, perhaps as early as phase +150 d. The one possible exception to the $M_{Co}(t)^2$ trend is SN 1991T, which appears to have a shallower evolution than the other SNe Ia. As we show below (Section 4.3), this cannot arise from gamma-ray opacity. Instead, the most likely explanation is probably a higher ionization state at early epochs ($t \leq 300$ d). Indeed, the spectra of SN 1991T near maximum light showed higher ionization in Fe than normal SNe Ia (Filippenko et al. 1992b). Interestingly, other SNe Ia with very high stretch in our sample (such as SN 2013aa) do not exhibit such behaviour either at maximum light (for SN 2013aa; Maguire et al. 2013) or in the nebular phase (i.e. Fig. 4). Because of this, for SN 1991T *only* we excise epochs prior to 300 d when calculating its ^{56}Ni mass in Section 5.2 – a choice which yields more favourable agreement with previous analyses from the literature.
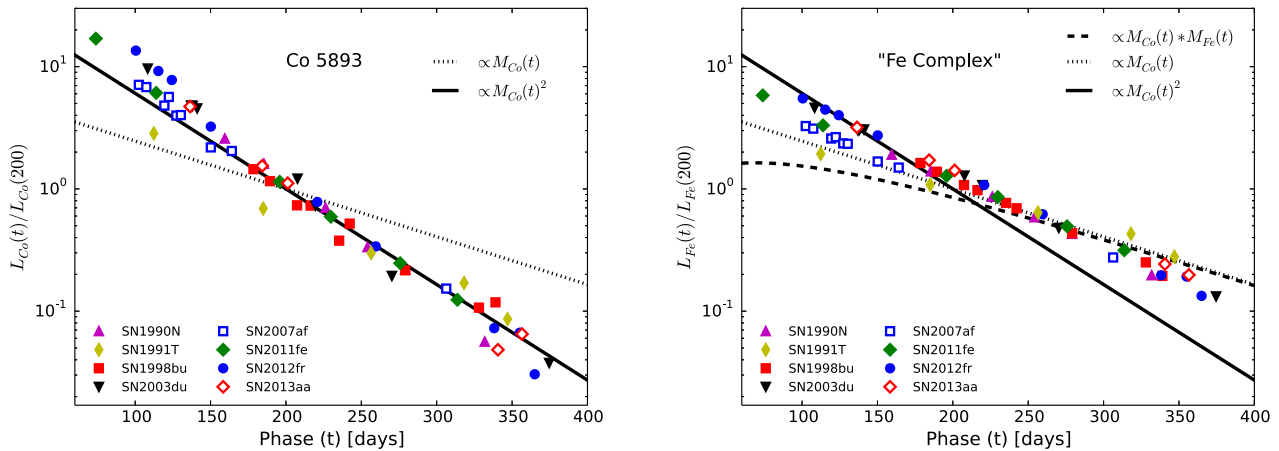
Figure 4. Left: evolution of the [Co III] λ5893 line flux in SNe Ia with nebular time series (≥3 observations past 150 d), compared to curves following the mass of ^{56}Co as a function of time to the first power (dotted line) and second power (solid line). Data for each SN was shifted by a multiplicative offset (i.e. log additive offset) that reduced residuals with the $M_{Co}(t)^2$ line. Right: evolution of the 'Fe complex' flux with phase, compared to the same lines as above as well as an additional line proportional to the product of the ^{56}Co mass and the ^{56}Fe mass as a function of time (dashed curve).

To contrast the behaviour of the [Co III] λ5893 line with other regions of the nebular spectra, we also inspected the evolution of the blue 'Fe complex' of lines. For each spectrum, we integrate the flux in the region 4100–5600 Å (adjusted for each SN according to its central nebular velocity measured from the Co line) where the emission is almost entirely dominated by Fe lines (see Fig. 2). Following our arguments for the expectation of the [Co III] λ5893 line flux, the Fe complex flux should be proportional to the energy being deposited – which scales as $M_{Co}(t)$ – and the mass fraction of Fe (which is nearly constant as $M_{Co} \ll M_{Fe}$ at this point). Thus, the Fe complex flux should scale with $M_{Co}(t) \times M_{Fe}(t) \approx M_{Co}(t)$. In the right-hand panel of Fig. 4, we plot the evolution of the Fe flux for the sample of SNe Ia, and see that it follows more closely the $M_{Co}(t)$ curve than the $M_{Co}(t)^2$ curve. However, we do note deviation from this line such that the logarithmic slope is somewhat intermediate between 1 and 2. Additionally, earlier epochs are subject to a complicated interplay of additional energy deposition from gamma-rays (as for the [Co III] λ5893 line, see Section 4.3), decreased emission due to non-zero optical depth in this region of the spectrum, and possible emission from Co II (see Fig. 2).

We note that the above results also explain one aspect of the data presented in Förster et al. (2013). Those authors examined the late ($35 \lesssim t \lesssim 80$ d) colour evolution (i.e. Lira law) for a large sample of nearby SNe Ia and its relationship with dust absorption (as inferred from narrow sodium absorption). The *B*-band decline rates were roughly 0.015 mag d^{-1}, while the *V*-band decline rates were nearly twice that (0.030 mag d^{-1}). The *B* band is dominated by the Fe complex whose flux decays as $M_{Co}(t)$, while the *V* band is heavily influenced by Co lines (see Fig. 2) whose flux decays as $M_{Co}(t)^2$. This naturally explains why the luminosity decay rate (in mag d^{-1}) in the *V* band is nearly twice that of the *B* band, and contributes to why SNe Ia become bluer (in $B - V$) with time at these epochs.

4.3 Testing gamma-ray opacity effects on [Co III] λ5893 evolution

While the data appear to agree with an $M_{Co}(t)^2$ dependence of the [Co III] λ5893 flux evolution, it is important to investigate the impact

of gamma-ray energy deposition on deviation from this parametrization.

To this end, we isolated the subset of SNe Ia from our sample with at least one nebular spectrum *earlier* than +150 d and at least one spectrum *later* than +250 d. For the six SNe Ia satisfying these criteria, we fit the [Co III] λ5893 flux evolution using the parametrization of equation (4). This fit has two free parameters: a multiplicative scaling for all the line fluxes, and the gamma-ray 'crossing' time t_c when energy deposition from gamma-rays and that from positrons are equal. These fits are shown in Fig. 5.

In general, the [Co III] λ5893 evolution is extremely well fitted by this model, especially for SNe Ia with good temporal coverage and high-S/N data (notably SN 2011fe and SN 2012fr). Some SNe Ia have a gamma-ray crossing time similar to the prediction from our model ($t_c \sim 200$ d) while some other SNe Ia have shorter crossing times ($t_c \sim 80$ d). The implications of this for SN Ia progenitors will be discussed in further detail in Section 6.1. Given these gamma-ray opacity model fit results, we calculate that deviations of [Co III] λ5893 flux evolution from the simple $M_{Co}(t)^2$ could range from 15 to 100 per cent at $t = 150$, 7 to 55 per cent at $t = 200$, and 4 to 30 per cent at $t = 250$ d.

5 MEASURING ^{56}NI MASS FROM SN IA NEBULAR SPECTRA

5.1 Placing [Co III] λ5893 flux measurements at disparate epochs on a common scale

To place all our SN Ia [Co III] λ5893 fluxes on a common scale, we first convert the observed line flux to the absolute line luminosity emitted by the SN using the distance to the SN host galaxy. For some SNe Ia in our sample, redshift-independent distance measurements exist for the host galaxy, particularly a number with Cepheid distance measurements. For most of the SNe Ia in our sample, however, the SN distance is computed by converting the host galaxy redshift to a distance using a Hubble constant value of $H_0 = 73.8$ km s^{-1} Mpc^{-1} chosen from Riess et al. (2011) to maintain consistency with those hosts with Cepheid distances from that work. For hosts with redshift-based distances, we assign a distance uncertainty corresponding to a peculiar velocity uncertainty
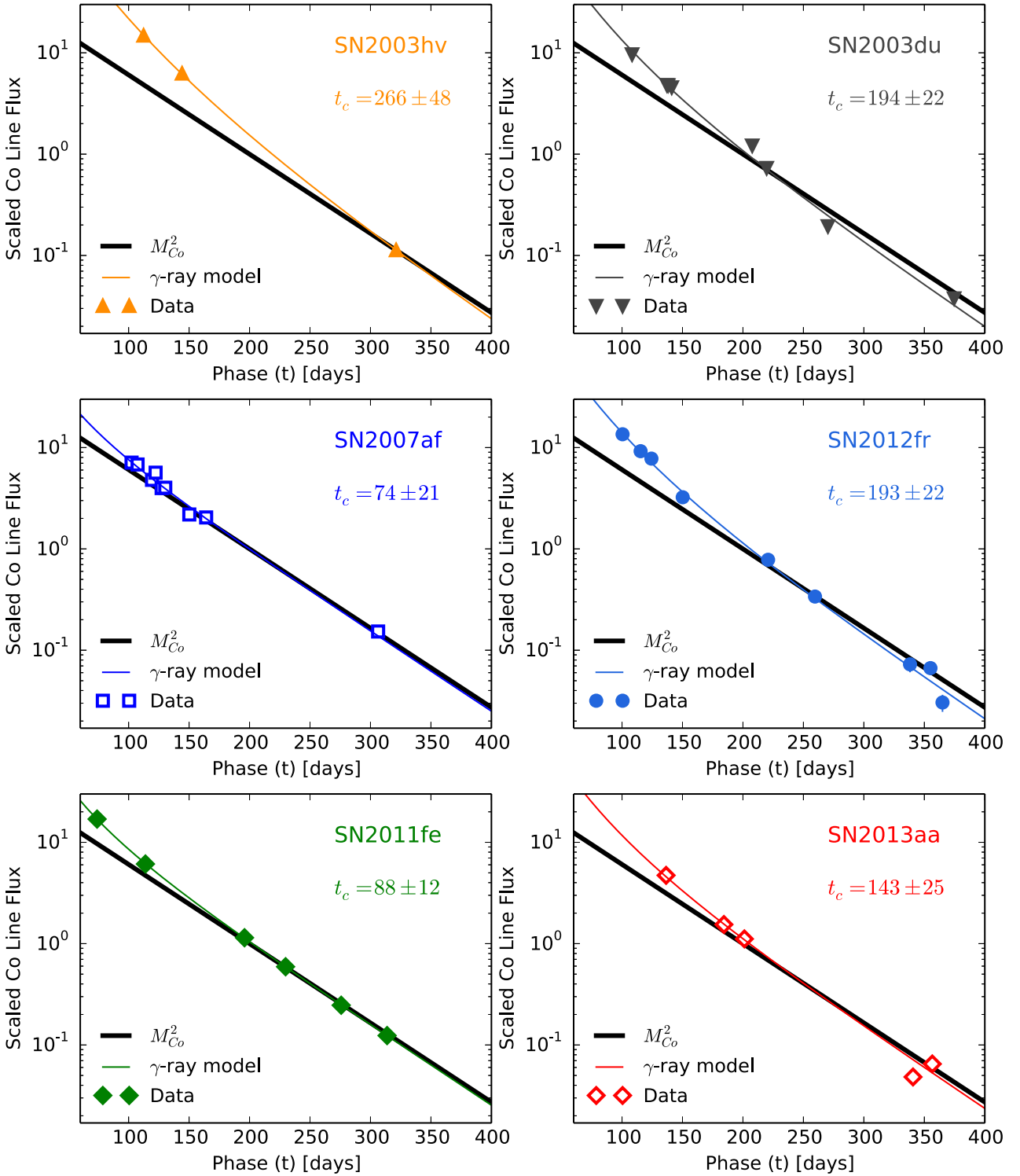
Figure 5. Fits of gamma-ray opacity model to select SN Ia [Co III] λ5893 line fluxes. The fitted 'crossing' time (when gamma-ray and positron energy deposition are equal) is shown in each panel.

of 300 km s^{-1}. Table B1 lists the full set of distance moduli (and references) employed in our sample.

Calculating the absolute [Co III] λ5893 flux emitted by each SN also requires correction for extinction by interstellar dust in the SN host galaxy. We accomplish this by calculating the Cardelli, Clayton & Mathis (1989, hereafter CCM) reddening curve at the rest

central wavelength of the [Co III] λ5893 complex for an appropriate value of the reddening $E(B - V)$ and selective extinction R_V. For most SNe Ia in our sample, the reddening is extremely low ($E(B - V) \leq 0.10$ mag), so we use the light-curve colour fitted by SiFTO (Conley et al. 2008), and a selective extinction value of $R_V = 2.8$ (appropriate for cosmological SNe Ia; see Chotard
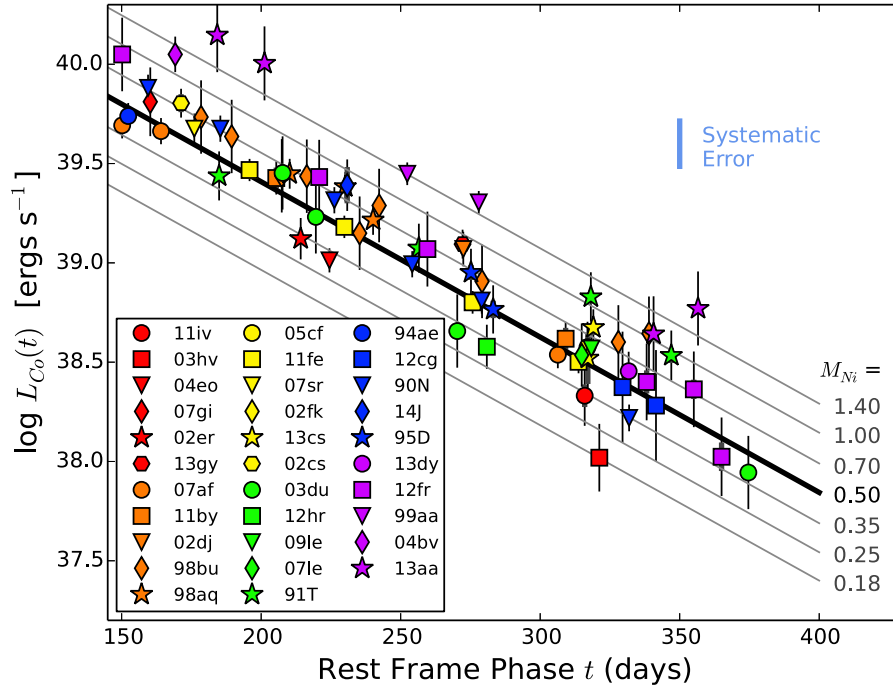
Figure 6. Evolution of the *absolute* [Co III] λ5893 line luminosity as a function of phase for all SNe Ia in our sample. The dark solid line corresponds to a ^{56}Ni mass of $M_{Ni} = 0.5\,M_\odot$ (the anchor value set by SN 2011fe), while the fainter grey lines represent other values of ^{56}Ni mass (labelled to right). Here thick error bars correspond to flux measurement errors, while narrow error bars correspond to distance uncertainties.

et al. 2011). We note that the choice of R_V has negligible impact on the majority of our sample. SN Ia light-curve colours are affected by both intrinsic colour and host galaxy extinction (see, e.g., Scolnic et al. 2014), so for SNe Ia with negative SiFTO colours – indicating blue intrinsic colours – we apply no colour correction (i.e. colour corrections never *redden* the data). In this work, we are not trying to standardize SN Ia (in which applying a colour correction to the intrinsic colours may also be appropriate); rather we are only concerned with eliminating the effects of dust extinction.

Two SNe Ia in our sample, however, have strong extinction by unusual dust and thus must be treated differently. SN 2014J occurred behind a thick dust lane in the nearby starburst galaxy M82. Foley et al. (2014) performed a detailed fit of multi-colour photometry of the SN, and find it is best fitted by a CCM-like reddening curve with $E(B - V) = 1.19$ and $R_V = 1.64$. We adopt their colour correction for SN 2014J, and for the line flux uncertainty arising from the reddening correction we adopt their uncertainty for the visual extinction of $\sigma_{A_V} = 0.18$ mag. SN 2007le showed moderately low extinction but with some variability in the sodium absorption feature likely arising from interaction of the SN with its circumstellar medium (Simon et al. 2009). Despite this variability, *most* of the absorption strength remains stable, so we adopt a colour correction for SN 2007le with $E(B - V) = 0.277$ and $R_V = 2.56$ as derived by Simon et al. (2009).

Fig. 6 presents the total emitted [Co III] λ5893 luminosity as a function of phase for all nebular spectra in our final sample. In this and subsequent figures, the thick error bars represent the composite measurement errors from the [Co III] λ5893 flux, *B*-band flux in the spectrum, observed (photometric) *B*-band magnitude, and extinction correction; the narrow error bars represent the distance uncertainties. Points are colour-coded (in groups) based on the light-curve stretch.

The line luminosity values are then used to compute an *effective* luminosity of the [Co III] λ5893 line at a common phase of +200 d for all SNe Ia in the sample (henceforward we refer to this as L_{Co}) using the M_{Co}^2 curve. For a single nebular spectrum, this can be calculated directly using the ^{56}Co decay lifetime:

$$\log(L_{Co}(200)) = \log(L_{Co}(t)) + 7.80 \times 10^{-3} * (t - 200). \quad (5)$$

For SNe Ia with multiple spectra, L_{Co} is calculated as the χ^2-weighted mean value across all acceptable epochs ($150 \le t \le 400$ d) using the above equation. We note that the above equation is calculated assuming a time between explosion and *B*-band peak (i.e. rise time) of 17 d, but there may be an associated uncertainty on this due to diversity in SN Ia rise times (Ganeshalingam et al. 2010) and possible dark phase before first light escapes (Piro & Nakar 2013). Each day of difference in explosion date results in a corresponding change in the final [Co III] λ5893 luminosity of 1.8 per cent – assuming an explosion date uncertainty of about 3 d, we thus expect that the explosion date uncertainty contributes about 5 per cent uncertainty to the final nickel mass derived in Section 5.2.

As noted in Section 4, SN 1991T may represent a case where the stable ionization state is not established until later than other SNe (also evident in Fig. 6), so for this SN we use the later two epochs ($t \ge 300$) to establish L_{Co}. This also yields favourable agreement of our ^{56}Ni mass with literature estimates (see Section 5.2).

In Fig. 7, we show the scaled $t = 200$ d [Co III] λ5893 line luminosity plotted against light-curve stretch. A clear correlation (Pearson $r = 0.66$) is evident between the [Co III] λ5893 line luminosity and stretch – this is expected given that the [Co III] λ5893 luminosity traces the amount of ^{56}Ni produced in the explosion, and ^{56}Ni directly powers the peak luminosity which correlates with the light-curve stretch.
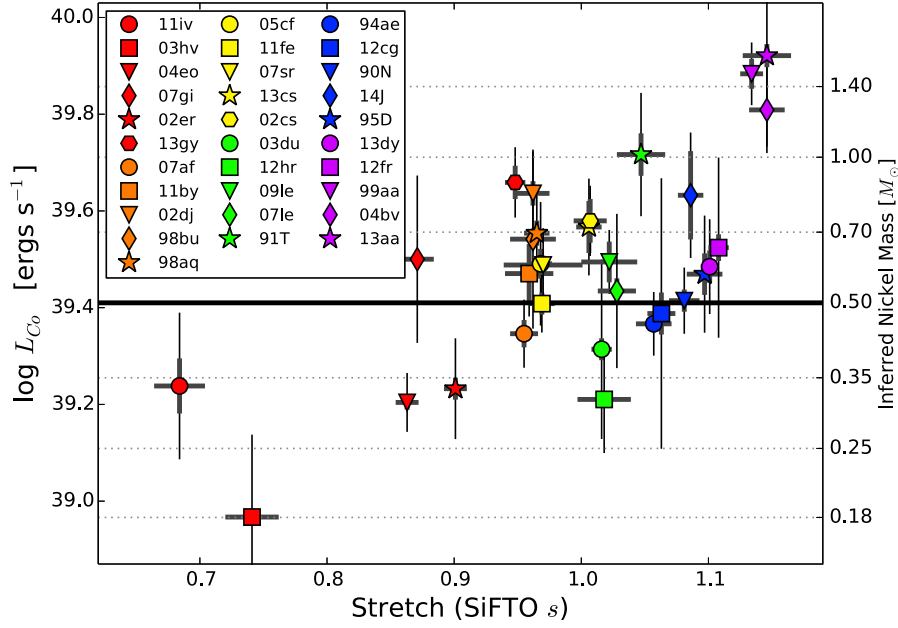
Figure 7. [Co III] λ5893 line luminosity scaled to its equivalent value at $t = 200$ d using the $M_{Co}(t)^2$ curve (L_{Co}) versus SN light-curve stretch. As in Fig. 6, thick error bars correspond to flux measurement errors, while narrow error bars correspond to distance uncertainty arising from peculiar velocities.

5.2 Inferring M_{Ni} from [Co III] λ5893 flux

Scaling the [Co III] λ5893 flux values to the same phase ($t = 200$ d) effectively places all measurements at the same epoch since explosion, so the amount of ^{56}Co will have the same proportionality to the amount of ^{56}Ni produced in the explosion. The final critical ingredient for inferring ^{56}Co mass (and thus ^{56}Ni mass) from the [Co III] λ5893 line flux is the scaling between ^{56}Co mass and [Co III] λ5893 flux. For reasons we will explore in Section 6.2, we expect this conversion factor to be relatively stable in time (for phases $150 \leq t \leq 400$ d considered here) and consistent across all SNe Ia. At these phases, we also expect ^{56}Co to be the dominant isotope (by mass) of cobalt (Seitenzahl, Taubenberger & Sim 2009a), as ^{57}Co only dominates energy deposition around $t \sim 1000$ d (Graur et al. 2015).

We expect the [Co III] λ5893 line flux at phase $t = 200$ d to be linearly proportional to the mass of ^{56}Ni produced in explosion (since the ^{56}Co mass fraction at this same epoch is necessarily the same for all SNe Ia). To convert [Co III] λ5893 flux to ^{56}Ni mass requires some scaling between the two quantities to be determined. In principle, this could be computed through radiative transfer modelling of late phases for SN Ia explosion models. However, for simplicity in this work, we choose to anchor the relation with the well-studied SN Ia SN 2011fe. Modelling of the photospheric phase light curve for SN 2011fe by Pereira et al. (2013) yielded a ^{56}Ni mass of $M_{Ni} = 0.53 \pm 0.11 \, M_{\odot}$. Recently, Mazzali et al. (2015) extended their spectroscopic modelling of the SN 2011fe spectral time series (presented for photospheric epochs in Mazzali et al. 2014) to nebular phase epochs and found $M_{Ni} = 0.47 \pm 0.08 \, M_{\odot}$. For simplicity in this work, we thus will choose a ^{56}Ni mass anchor for SN 2011fe of $M_{Ni} = 0.50 \, M_{\odot}$, yielding final ^{56}Ni mass values derived as

$$M_{Ni} = 0.50 \, M_{\odot} \frac{L_{Co}}{L_{11fe}}, \tag{6}$$

where $\log(L_{11fe}) = 39.410$ is the scaled [Co III] λ5893 luminosity we measure for SN 2011fe – this is used as a zero-point for the

remainder of our SN sample. The values for M_{Ni} for our sample are presented in Table 3. In Section 6.3, we further discuss the implications of our ^{56}Ni mass values and their relation to the ejected masses of our SN Ia sample.

Other techniques have been presented for measuring the mass of ^{56}Ni produced in the SN Ia explosion. Stritzinger et al. (2006a) employed semi-empirical modelling of SN Ia bolometric light curves to measure the ejected mass and ^{56}Ni mass for a sample of 17 nearby SNe Ia. They then found that ^{56}Ni masses derived from modelling of the nebular spectra (Mazzali et al. 1997, 1998; Stehle et al. 2005) yielded consistent results (Stritzinger et al. 2006b). Seven of the SNe Ia from their sample are included in ours, and we show a comparison of our ^{56}Ni values versus those derived from their two methods in Fig. 8. In some of the cases, our ^{56}Ni masses are somewhat lower than theirs (both for the light curve and nebular ^{56}Ni mass estimates) though generally show acceptable agreement. We note that for SN 1994ae and SN 2002er, Stritzinger et al. (2006b) employ a much higher reddening value than ours ($E(B - V) = 0.15$ mag versus $E(B - V) = 0.00$ mag for SN 1994ae and $E(B - V) = 0.36$ mag versus $E(B - V) = 0.12$ mag for SN 2002er), which is likely the source of the discrepancy between our values.

6 DISCUSSION

In this Section, we discuss the important physical implications of our observational results above. First, we examine the fact that the [Co III] λ5893 line flux evolution requires a constant scaling between energy released by ^{56}Co decay and that absorbed by the nebula – this requires efficient local deposition of energy from positrons and near-complete escape of gamma-rays from the IGE core (Section 6.1). Next, we argue that the [Co III] λ5893 evolution requires stable ionization conditions in the nebula for a period of several hundred days, which we support by demonstrating stability of ionization-dependent flux ratios measured from the data (Section 6.2). Finally, we discuss potential interpretations of SN Ia explosion conditions

Table 3. Final SN Ia nickel masses.

SN	M_{Ni} ($M_\odot$)[a]	M_{ej} ($M_\odot$)[b]
SN 1990N	$0.507 \pm 0.027 (0.080)$	1.437 ± 0.009
SN 1991T	$1.017 \pm 0.103 (0.298)$	1.407 ± 0.019
SN 1994ae	$0.454 \pm 0.013 (0.069)$	1.417 ± 0.013
SN 1995D	$0.575 \pm 0.057 (0.160)$	1.448 ± 0.009
SN 1998aq	$0.699 \pm 0.042 (0.126)$	1.304 ± 0.015
SN 1998bu	$0.680 \pm 0.029 (0.290)$	1.299 ± 0.027
SN 1999aa	$1.493 \pm 0.106 (0.223)$	1.465 ± 0.003
SN 2002cs	$0.741 \pm 0.077 (0.124)$	1.361 ± 0.016
SN 2002dj	$0.845 \pm 0.049 (0.169)$	1.299 ± 0.019
SN 2002er	$0.334 \pm 0.017 (0.080)$	1.202 ± 0.015
SN 2003du	$0.402 \pm 0.021 (0.172)$	1.373 ± 0.010
SN 2003hv	$0.181 \pm 0.003 (0.071)$	0.914 ± 0.037
SN 2004bv	$1.257 \pm 0.039 (0.259)$	1.468 ± 0.003
SN 2004eo	$0.312 \pm 0.011 (0.044)$	1.135 ± 0.016
SN 2005cf	$0.604 \pm 0.043 (0.178)$	1.308 ± 0.013
SN 2007af	$0.433 \pm 0.028 (0.070)$	1.289 ± 0.017
SN 2007gi	$0.618 \pm 0.027 (0.246)$	1.149 ± 0.023
SN 2007le	$0.531 \pm 0.032 (0.195)$	1.387 ± 0.017
SN 2007sr	$0.601 \pm 0.027 (0.105)$	1.311 ± 0.045
SN 2009le	$0.610 \pm 0.059 (0.093)$	1.380 ± 0.026
SN 2011by	$0.577 \pm 0.081 (0.118)$	1.295 ± 0.029
SN 2011fe	$0.500 \pm 0.026 (0.069)$	1.310 ± 0.015
SN 2011iv	$0.338 \pm 0.044 (0.118)$	0.818 ± 0.032
SN 2012cg	$0.477 \pm 0.048 (0.307)$	1.422 ± 0.010
SN 2012fr	$0.653 \pm 0.041 (0.280)$	1.454 ± 0.004
SN 2012hr	$0.317 \pm 0.008 (0.081)$	1.375 ± 0.025
SN 2013aa	$1.628 \pm 0.090 (0.704)$	1.468 ± 0.004
SN 2013cs	$0.720 \pm 0.089 (0.166)$	1.360 ± 0.013
SN 2013dy	$0.596 \pm 0.046 (0.135)$	1.450 ± 0.004
SN 2013gy	$0.890 \pm 0.070 (0.149)$	1.278 ± 0.012
SN 2014J	$0.838 \pm 0.176 (0.250)$	1.441 ± 0.007

Notes. [a]Nominal uncertainties arise from measurement errors in the Co line flux or SN reddening, while distance uncertainties are listed in parentheses. Systematic error for M_{Ni} is estimated at $0.2\,M_\odot$.
[b]Includes only measurement uncertainties from SN light-curve stretch. Systematic error for M_{ej} is estimated at $0.1\,M_\odot$.

implied by our observed relationship between inferred ^{56}Ni mass and ejected mass (Section 6.3).

6.1 Gamma-ray transparency time-scales for nebular SNe Ia

For ^{56}Co to deposit a constant fraction of its decay energy into the nebula, positrons from the decay must be efficiently trapped in the IGE core and gamma-rays must be able to effectively escape.[3] As noted above, efficient local positron energy deposition is expected to hold for the temperatures and densities encountered at these nebular phases (Axelrod 1980; Chan & Lingenfelter 1993; Ruiz-Lapuente & Spruit 1998). In practice, gamma-rays become negligible after the time when the gamma-ray energy deposition equals that from positrons, which occurs when the optical depth drops enough to reach this equality (Section 4.1). We will refer to this henceforth as the 'transparency' time-scale t_c – after this epoch, positrons dominate energy deposition in the nebula.

[3] We do note that other physical properties of the nebula (e.g. ionization or emission measure changes) could somehow conspire to compensate for gamma-ray opacity to make the line emission evolve as M_{Co}^2, but we consider the gamma-ray transparency scenario to be the simplest explanation.
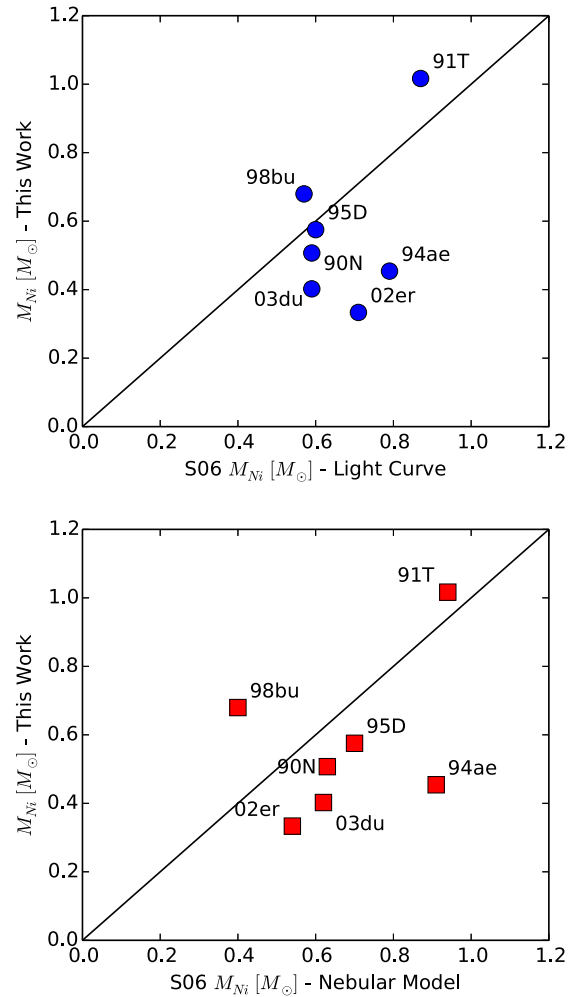
Figure 8. Comparison of our ^{56}Ni mass values to those derived by Stritzinger et al. (2006b) using light-curve modelling (left) and nebular spectra modelling (right).

We fit the transparency time-scale for several SNe in Section 4.3 and found that several have longer transparency times ($t_c \sim 180$ d) close to the theoretical expectation for the DDC10 model. Previous analysis of gamma-ray transparency time-scales found similar results: $t_c \approx 170$ d for SN 2000cx (Sollerman et al. 2004) and $t_c \approx 188$ d for SN 2001el (Stritzinger & Sollerman 2007). However, we found that other SNe Ia (notably SN 2011fe and SN 2007af) had much shorter transparency times ($t_c \sim 80$ d). This variation in transparency times may reflect a diversity in nebular densities, as most of the gamma-ray opacity at these late epochs will come from opacity from electrons in the nebula. Interestingly, the SNe Ia with shorter transparency times (SN 2011fe and SN 2007af) have lower stretch values than most of the SNe Ia with longer transparency times (SN 2003du, SN 2012fr, SN 2013aa), possibly indicating some relationship between nebular density and stretch. The one exception to this is SN 2003hv, which appears to have low stretch but long transparency time (and thus would imply high density) – this result is opposite to the findings of Mazzali et al. (2011) who found that SN 2003hv had reduced density in the inner regions of the ejecta. The source of this discrepancy is unclear, but may constitute further evidence that SN 2003hv is a 'non-standard' event.

Because of the diversity in gamma-ray transparency time-scales in the SNe Ia we tested, it is likely that the impact of gamma-ray energy deposition on the [Co III] λ5893 flux will be impacted by similar variability. Given the results above (Section 4.3), this may result in an average uncertainty of 30 per cent on the final ^{56}Ni masses we infer (if we use $t = 200$ d as the mean measurement epoch). The only robust way to account for gamma-ray opacity effects is to obtain a nebular time series. However, the transparency time is best constrained by observations from 100 to 150 d (in addition to one later spectrum to anchor the M_{Ni} measurement) when the SN is only 3–4 mag fainter than peak. Thus, it should be observationally feasible to obtain such data for future SNe Ia observed in the nebular phase.

More interestingly, the time evolution of the [Co III] λ5893 flux presents a new method for measuring the gamma-ray transparency time-scale, as it gives a direct probe of the energy being deposited into the nebula. Previously, this could only be done with the aid of bolometric light curves (Sollerman et al. 2004; Stritzinger & Sollerman 2007; Leloudas et al. 2009), which necessarily rely on extensive optical and infrared photometry and/or uncertain bolometric corrections. Instead, our method requires only two nebular spectra with contemporaneous optical photometry.

6.2 Ionization conditions in the SN nebula

As noted above, the consistency of the [Co III] λ5893 flux evolution with the square of the cobalt mass implies a constant scaling between the energy being absorbed by cobalt atoms and the energy they emit in the [Co III] λ5893 line. This implies stability in the ionization

conditions of the nebula, which we now investigate from a more detailed inspection of our nebular spectra.

To confirm that the ionization state of the nebula is indeed slowly evolving within phases $150 \leq t \leq 400$ d, we examine the flux ratios of nebular emission lines arising primarily from Fe II and Fe III: the 4700 Å complex dominated by Fe III, the 4200 Å complex which is dominated by Fe II, and the 5270 Å complex which is a blend of Fe II and Fe III. If the ratio of these lines evolves with time, this would indicate a change in the ionization state. In the left-hand panels of Fig. 9, we highlight the regions of the typical SN Ia nebular spectra (here from SN 2011fe and SN 2012fr) which are dominated by strong line complexes of either Fe II or Fe III. We integrate the flux in these regions for all the nebular SN Ia spectra in our sample, and in the right-hand panels of Fig. 9 we show how the line flux ratios evolve with phase for the nebular time series SNe Ia (the same as from Section 4.2). For this analysis, we only consider phases later than $t \sim 200$ d, as this is when this region of the spectrum is reliably optically thin (see Section 4) – note that this cuts SN 2007af from the Fe time series sample.

Though there is indeed some evolution in the flux ratio of Fe II lines to Fe III lines, it is comparatively small – for each individual SN, the line flux ratios generally change by less than 10 per cent of the relative line flux in Fe III compared to Fe II (with the possible exception of SN 1990N). We perform a simple linear fit to the evolution of the line flux ratios for each SN in Fig. 9, and from the mean slope of these fits we measure the mean evolution of the line flux ratios for the SNe Ia in this sample to be 2.7 per cent per 100 d and 7.3 per cent per 100 d for the 4700/4200 and 4700/5270 flux ratios, respectively.
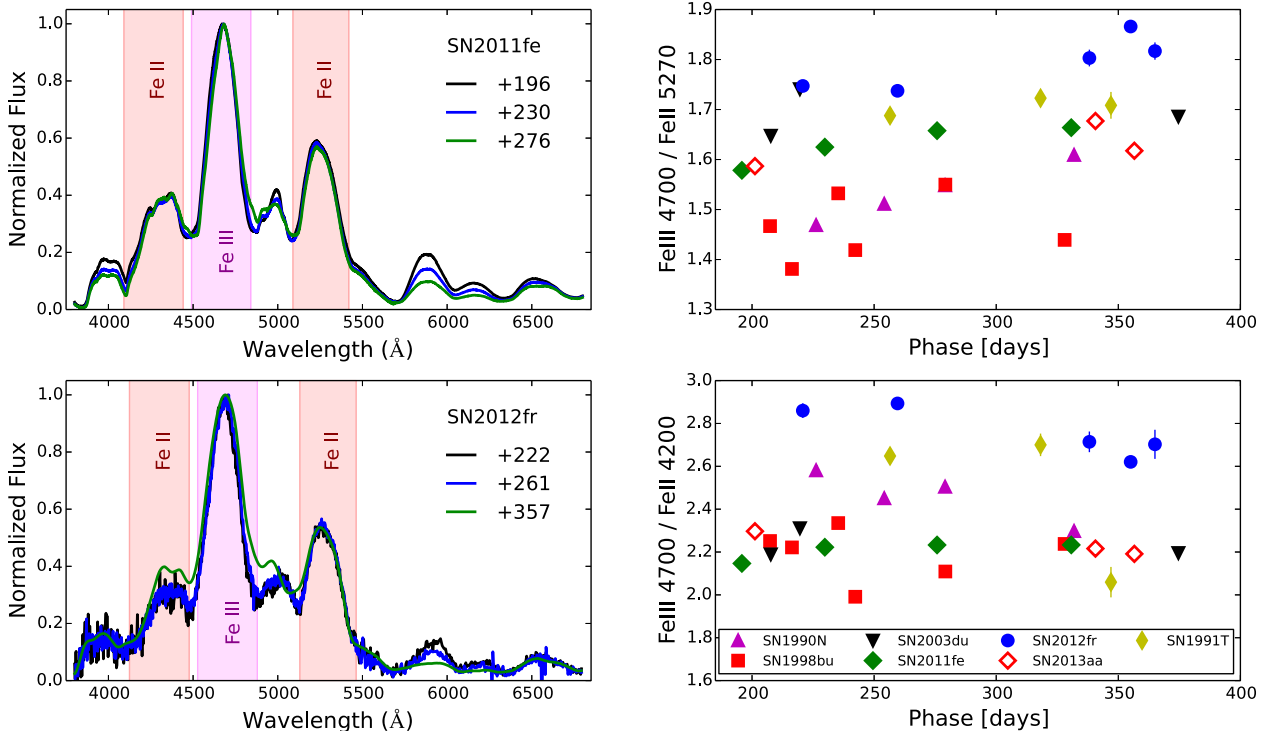

Figure 9. Left-hand panels: multiple nebular phase spectra of SN 2011fe (top) and SN 2012fr (bottom), highlighting the flux integration regions for the line complexes dominated by Fe II (light red regions) and Fe III (light magenta regions). Integration zones are shifted by the central redshift of the nebular Fe lines: here a blueshift of ~600 km s^{-1} for SN 2011fe and a redshift of ~1800 km s^{-1} for SN 2012fr. Right-hand panels: temporal evolution of the ratios of the flux integral for the Fe III 4700 Å complex compared to the Fe II 5270 Å complex (top) and Fe II 4200 Å complex (bottom) for SNe Ia with nebular time series. In both panels, we show formal flux errors from the spectra, which are generally smaller than the data points.
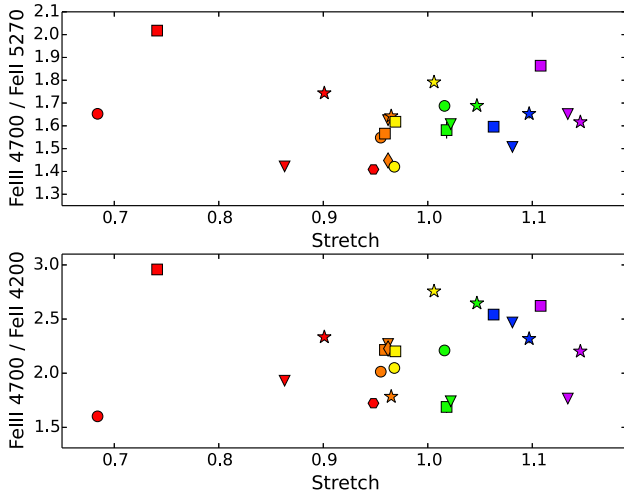
Figure 10. Integrated flux ratios of the Fe III 4700 Å complex compared to the Fe II 5270 Å complex (top) and Fe II 4200 Å complex (bottom) as a function of light-curve stretch (SiFTO *s*) for all SNe Ia in our sample. Formal spectrum flux error bars are smaller than the data markers. Markers are the same as for Fig. 7.

In sharp contrast, consider the Fe III/Fe II line flux ratios as measured from the $t \sim 1000$ d spectrum for SN 2011fe from Taubenberger et al. (2015) – 0.52 for 4700/5270 versus a mean of 1.6 at earlier phases, and 0.87 for 4700/4200 versus an earlier mean of 2.3 – which decrease by at least 65 per cent from their values in the $150 \leq t \leq 400$ d range (we note that these values should be considered upper limits as it appears that the Fe III 4700 line has effectively disappeared in the $t \sim 1000$ d spectrum for SN 2011fe, so the flux we measure here is likely due to other species). By these very late phases, the physical conditions in the SN Ia nebula have clearly changed in a dramatic fashion. Such is not the case for the SNe Ia in our sample at phases $150 \leq t \leq 400$ d.

In order to meaningfully compare the [Co III] λ5893 line flux from different SNe Ia, another key requirement is that the ionization state of *all* SNe Ia be relatively similar. To test this assumption, we again use the Fe line ratios described above, but plot the mean Fe III/Fe II line flux ratio (computed as the error-weighted mean for SNe Ia with multiple epochs) versus light-curve stretch in Fig. 10. We have excluded the highly reddened SN 2007le and SN 2014J to avoid any biases in these ratios due to uncertainty in the dust law (i.e. R_V).

Here we see some mild coherent change in the Fe line flux ratios (and thus ionization state) as a function of light-curve stretch (with SN 2003hv as an outlier, as previously noted by Mazzali et al. 2011). If we exclude SN 2003hv and perform a linear fit to the flux ratio trends with stretch, our best-fitting slope implies an evolution of the 4700/4200 and 4700/5270 flux ratios of 6 and 25 per cent, respectively, over the range $s = 0.7$–1.1. We measure a scatter of 15 and 7 per cent for these two ratios, respectively. The ionization potentials of Fe and Co are very similar, which means a change in Fe III line flux induced by variation of the ionization state will manifest a comparable change in Co III line flux. Thus, we estimate that our [Co III] λ5893 line fluxes above should have an additional scatter due to ionization state variations of about 15 per cent. Since our inferred ^{56}Ni masses are proportional to this line flux, this means that ionization state variations could induce a scatter of similar magnitude in our ^{56}Ni masses.

Our measurement of the [Co III] λ5893 line flux evolution, and variations of Fe III/Fe II line flux ratios as a function of both phase

and SN stretch, coherently indicates that the ionization states of normal SNe Ia are remarkably consistent across different SNe and nearly constant across phases $150 \leq t \leq 400$ d. This stability of the ionization state was predicted by Axelrod (1980), and our results here present the most compelling evidence to date in support of that prediction.

6.3 The relationship between ^{56}Ni and ejected mass

The relationship between [Co III] λ5893 luminosity and light-curve stretch (Fig. 7) hints at a relationship between physical properties of the SN Ia progenitor system. In Section 5.2, we converted our measured [Co III] λ5893 line luminosities into inferred ^{56}Ni masses. Here we convert light-curve stretch into the SN ejected mass (i.e. progenitor mass for SNe Ia) using the relationship between M_{ej} and light-curve stretch discovered by Scalzo et al. (2014a). Scalzo et al. (2014b) used Bayesian inference to model the intrinsic distribution of ejected masses, which can be folded in as an additional prior when determining ejected mass using this relation. We derive a cubic fit to the relationship between stretch and M_{ej}:

$$M_{ej} = 2.07 - 7.51s + 11.56s^2 - 4.77s^3$$
$$= 1.35 + 1.30(s - 1) - 2.75(s - 1)^2 - 4.77(s - 1)^3. \quad (7)$$

The resultant values for ejected mass (M_{ej}) we derive are presented in Table 3 along with our ^{56}Ni masses.

In Fig. 11, we plot our inferred ^{56}Ni masses against these ejected masses. We note that there is a systematic uncertainty associated with M_{ej} calculation of about 0.1 $M_\odot$, as determined by Scalzo et al. (2014a) from recovering masses of SN Ia explosion models. For ^{56}Ni masses, we previously noted several sources of uncertainty: 10 per cent uncertainty in the [Co III] λ5893 flux itself (Section 3.2), 5 per cent uncertainty on the $t = 200$ [Co III] λ5893 luminosity due to uncertainty in the explosion date (Section 5.1), 15 per cent from ionization state variations (Section 6.2), and possibly 30 per cent from variations in gamma-ray transparency time-scales (Section 6.1). Collectively this constitutes a possible 35 per cent uncertainty in our ^{56}Ni masses, which given the values we find would produce a mean uncertainty in M_{Ni} of about 0.2 $M_\odot$.

The relation between M_{Ni} and M_{ej} shows potential evidence for two regimes for the production of ^{56}Ni in SNe Ia. Indeed, if we split the sample at $M_{ej} = 1.3 M_\odot$, a Kolmogorov–Smirnov test yields $D = 0.40$ (note that this is twice the mean systematic uncertainty in M_{Ni} of 0.2 $M_\odot$) which for this sample size implies a likelihood of M_{Ni} values drawn from the same distribution of only 16 per cent. For sub-Ch ejected masses ($M_{ej} \lesssim 1.3 M_\odot$ – though note that SN 1991bg-like objects are not included in this analysis), the amount of ^{56}Ni produced is clustered around $M_{Ni} \sim 0.4 M_\odot$, with a possible increase of M_{Ni} with M_{ej} (though we note that the statistics are small). Chandrasekhar-mass progenitors ($M_{ej} \approx 1.4 \pm 0.1 M_\odot$) produce ^{56}Ni masses in the range $0.4 M_\odot \lesssim M_{Ni} \lesssim 1.2 M_\odot$, with the extreme high ^{56}Ni masses ($M_{Ni} \gtrsim 1.0 M_\odot$) occurring in SNe Ia which are highly luminous and spectroscopically peculiar: SN 1991T (Filippenko et al. 1992b), SN 1999aa (Garavini et al. 2004), SN 2004bv (Silverman et al. 2012a), and SN 2013aa (Maguire et al. 2013). Recently, Fisher & Jumper (2015) suggested that Chandrasekhar-mass SN Ia progenitors preferentially lack a vigorous deflagration phase following the initial ignition, and result in a nearly pure detonation that produces about 1.0 $M_\odot$ of ^{56}Ni and shows similarity to SN 1991T. Our findings that the [Co III] λ5893 luminosity is exceptionally high only in 91T-like SNe Ia (Fig. 11) could lend support to this theory.

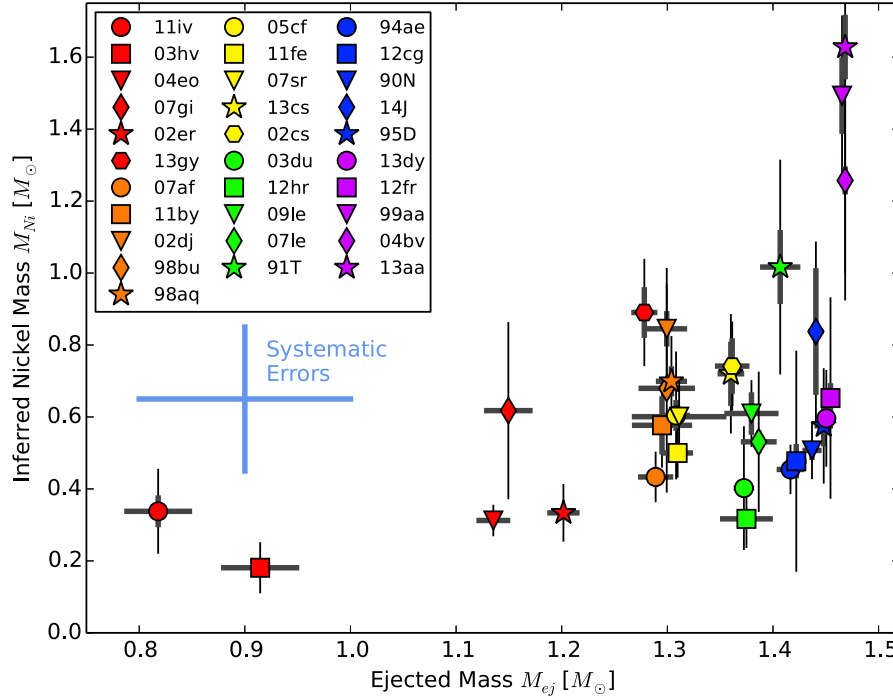**Figure 11.** Mass of ^{56}Ni inferred from the scaled [Co III] $\lambda 5893$ line luminosity versus total ejected mass (i.e. progenitor WD mass) inferred from SN light-curve stretch. As in Fig. 6, thick error bars correspond to flux measurement errors (including colour correction uncertainties), while narrow error bars correspond to distance uncertainties arising from peculiar velocities. The typical systematic uncertainties for estimating M_{ej} ($\pm 0.1\,M_\odot$ – from the stretch-M_{ej} relation of Scalzo et al. 2014b) and M_{Ni} ($\pm 0.2\,M_\odot$ – from gamma-rays, explosion date uncertainty, and possible line contamination) are shown as the blue error bars in the left side of the plot. Note the anomalously high M_{Ni} values for SN 1999aa and SN 2013aa, which we attribute to line contamination and distance uncertainty, respectively (see the text for details).

We note that SN 1999aa and SN 2013aa have anomalously high M_{Ni} values (indeed exceeding their M_{ej} values). We visually inspected the spectra of these SNe, and find no fault in our fits to the [Co III] $\lambda 5893$ line. SN 1999aa notably has the broadest line width of our sample, which could result in contamination of our measured [Co III] $\lambda 5893$ flux by nearby Fe II lines (see Fig. 2). SN 2013aa has a relatively uncertain distance to its host galaxy. We expect that the true M_{Ni} for these two SNe is likely to be closer to that of the other SN 1991T-like SNe Ia, near 1.0–1.2 $M_\odot$.

To compare model predictions with our inferred ^{56}Ni mass values, we gather ejected mass and ^{56}Ni mass outcomes from numerous SN Ia explosion models and plot them against our data in Fig. 12. These models can be generally grouped into three categories: sub-Ch mass detonations, Chandrasekhar-mass DDTs (DDT), and Chandrasekhar-mass deflagrations which fail to detonate. We discuss each category and its agreement with the data below.

Sub-Ch mass detonations: we consider sub-Ch detonations from Sim et al. (2010), where detonations were artificially initiated in WDs of varying initial masses. These models are also applicable to sub-Ch WDs ignited via other mechanisms (e.g. a violent merger), and were also employed to estimate the brightness distribution of violent mergers in Ruiter et al. (2013). We also examine sub-Ch DDet models from Fink et al. (2010): these are qualitatively similar to those from Sim et al. (2010) but the ignition mechanism naturally arises from a surface helium layer ignition. Both models show a similar relationship between M_{Ni} and M_{ej}, which shows a much steeper increase of M_{Ni} with M_{ej} than we infer from our data. However, we note that with the systematic uncertainty in M_{ej} estimates (from stretch) these may be compatible with the data.

Deflagration-to-detonation transitions (DDTs): we present models from both Seitenzahl et al. (2013a) and Blondin et al. (2013) – including the DDC10 model employed for radiative transfer calculations in Section 3.1. These models explicitly begin with an M_{Ch} progenitor (and thus have $M_{ej} = M_{Ch}$ by construction) which undergoes an initial deflagration phase that transitions to a detonation at a later time: the timing of this transition directly sets the amount of ^{56}Ni produced. For Seitenzahl et al. (2013a), the DDT time was calculated from the sub-grid-scale turbulent energy (Ciaraldi-Schoolmann, Seitenzahl & Röpke 2013) which in practice varied with the vigorousness of the initial deflagration (set by hand as the number of initial ignition points). For Blondin et al. (2013), the DDT time is set by a manual trigger. Both sets of models cover a range of ^{56}Ni mass production, similar to the range inferred from our data.

Pure deflagrations: finally, we consider pure deflagration models presented in Fink et al. (2014). These models are variations on the Chandrasekhar-mass Seitenzahl et al. (2013a) models in which the DDT module has been intentionally turned off. Many of these deflagration models fail to fully unbind the star and eject only a portion of the WD's total mass and leave a bound remnant – we note that the Scalzo et al. (2014b) method for estimating ejected mass from light curves is not trained to account for bound remnants so may have some additional systematic uncertainty for this explosion mechanism. Interestingly, these models show a weak dependence of M_{Ni} on M_{ej} for sub-Ch ejected masses, similar to what we infer for this regime of the data. This also shows some agreement with the WLR observed in cosmological SN samples – we show this as well in Fig. 12 using the WLR from Betoule et al. (2014) converted to M_{Ni} and M_{ej} using the relations presented in Scalzo et al. (2014b).
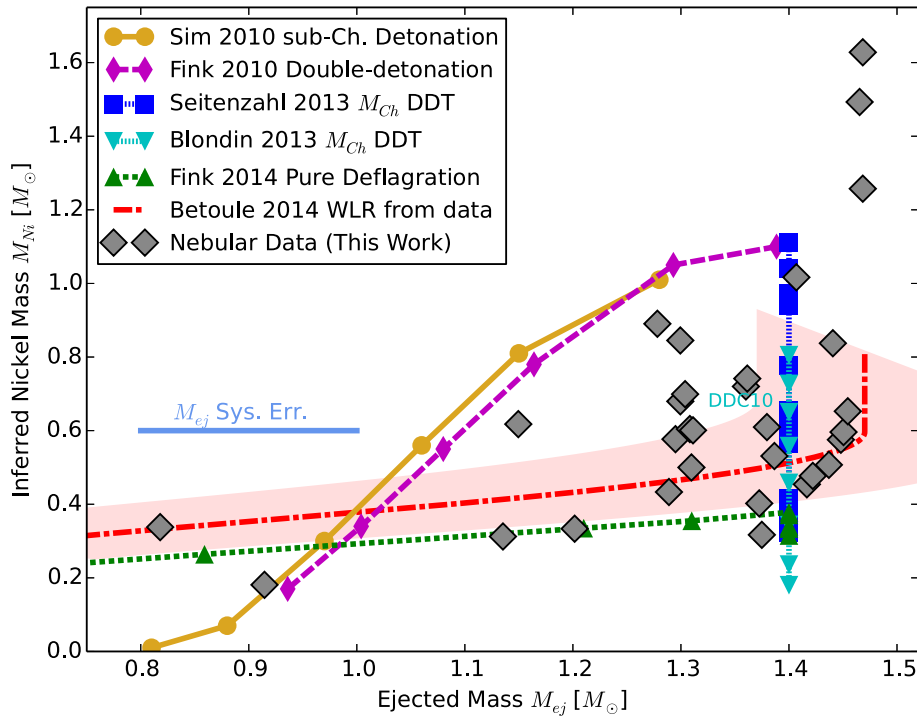
Figure 12. M_{Ni} and M_{ej} values inferred from data (dark grey diamonds – data as in Fig. 11) compared to various theoretical models: pure detonation models from sub-Ch detonations (Sim et al. 2010, yellow circles) and DDets (Fink et al. 2010, magenta diamonds); DDTs from Seitenzahl et al. (2013a, blue squares) and Blondin et al. (2013, cyan downward triangles) – the latter work includes the DDC10 model used for late-time spectral modelling in Section 3.1 and Fig. 2; and Chandrasekhar-mass pure deflagrations (Fink et al. 2014, green upward triangles). The observed WLR (and its scatter) from the recent cosmology analysis of Betoule et al. (2014) is shown as the red curve (and light red shaded area).

If indeed the M_{Ni}–M_{ej} trend arises from two distinct explosion mechanisms for SNe Ia, several key questions remain to be answered with future research. One such question is where the split between the two mechanisms occurs – SNe Ia at M_{Ch} with $\sim 0.5\,M_\odot$ of ^{56}Ni could arise from either mechanism – and what physical property of the progenitor decides which mechanism occurs. Next we should investigate why the two mechanisms produce SNe Ia which obey the same WLR – one might expect that a different relationship between M_{Ni} and M_{ej} would yield different relationship between peak luminosity and light-curve width. Such insights could be further advanced by study of other related thermonuclear explosions which span a broader range of M_{Ni} and M_{ej} (e.g. McCully et al. 2014b, see their fig. 15).

Finally, we most critically should assess whether the two mechanisms calibrate cosmological distances in the same fashion. Recent evidence has been mounting that SNe Ia show progenitor signatures (e.g. CSM interaction, high-velocity features, host galaxy properties) that appear to clump into two groups (Maguire et al. 2014), which may in turn be reflected in other observational behaviours such as UV colour (Milne et al. 2013, 2015). In parallel, SN Ia cosmological analyses have found that SNe Ia in high- and low-mass galaxies have subtly different standardized luminosities (Kelly et al. 2010, 2015; Lampeitl et al. 2010; Sullivan et al. 2010; D'Andrea et al. 2011; Gupta et al. 2011; Konishi et al. 2011; Galbany et al. 2012; Childress et al. 2013c; Hayden et al. 2013; Johansson et al. 2013; Rigault et al. 2013; Childress, Wolf & Zahid 2014c). These and the current study motivate further examination of the environments and standardized luminosities of SNe Ia whose ^{56}Ni mass and ejected mass are assessed with the techniques presented here. Such a study is limited by distance uncertainties, and thus should be targeted at SNe Ia in the nearby smooth Hubble flow ($z \geq 0.015$)

where distance uncertainties from peculiar velocities become small (≤ 0.10 mag).

7 CONCLUSIONS

In this work, we examine the [Co III] λ5893 feature in 72 nebular phase ($150 \leq t \leq 400$ d past peak brightness) spectra of 32 SNe Ia compiled from the literature and new observations. This feature arises predominantly from radioactive ^{56}Co, the decay product of ^{56}Ni (which powers the bright early light curve) – thus this feature provides a direct window for investigating the power source behind SN Ia light curves.

We used nebular time series for eight SNe Ia to show that the temporal evolution of the [Co III] λ5893 flux falls very close to the square of the mass of ^{56}Co as a function of time. This is the expected dependence in the limit where the nebula is fully optically thin to gamma-rays produced in the ^{56}Co decay but locally thermalizes energy from positrons emitted in the decay. We then used this uniform time dependence to infer the relative amount of ^{56}Ni produced by all 32 SNe Ia in our sample by using SN 2011fe as an anchor (at $M_{Ni} = 0.5\,M_\odot$).

The greatest systematic uncertainty in our ^{56}Ni mass measurements was the time at which the nebula becomes effectively optically thin to gamma-rays (which we define by the 'crossing' time when energy deposition from positrons begins to exceed that of gamma-rays). Though this could introduce 30 per cent uncertainty in ^{56}Ni masses (on average, though this is time dependent), we showed that the gamma-ray transparency time can be readily measured when multiple nebular spectra are available. In particular, a single additional spectrum at phases $100 \leq t \leq 150$ d past maximum light – when the SN is only 3–4 mag fainter than peak – can

easily constrain the gamma-ray transparency time when coupled to a later spectrum (which anchors the measurement of M_{Ni}). This can robustify our technique for measuring ^{56}Ni masses of future SNe Ia, but the gamma-ray transparency time itself could provide important clues to SN Ia progenitor properties.

When comparing our inferred ^{56}Ni masses to the ejected masses of our SN Ia sample (using techniques from Scalzo et al. 2014a,b), we find evidence for two regimes in the production of ^{56}Ni (which are too distinct to be an artefact of systematic uncertainties). For low ($M_{ej} \leq 1.3\,M_\odot$) ejected masses (low stretch), M_{Ni} clusters at low values ($M_{Ni} \approx 0.4\,M_\odot$). At high ejected masses (high stretch) near the Chandrasekhar mass, M_{Ni} has a much larger spread ($0.4\,M_\odot \lesssim M_{Ni} \lesssim 1.2\,M_\odot$). This could constitute evidence for two distinct explosion mechanisms in SNe Ia.

This work has illustrated the power of the nebular [Co III] $\lambda5893$ feature in probing the fundamental explosion physics of SNe Ia. We provide a simple recipe for calculating ^{56}Ni mass from the [Co III] $\lambda5893$ line flux from a single nebular epoch (equations 5 and 6), as well as prescription for a more robust measurement that accounts for opacity effects by using multiple nebular epochs (equation 4). Future measurements which eliminate the opacity systematics and distance uncertainties could provide a detailed understanding of the explosion mechanisms for SNe Ia.

REFERENCES

Aldering G. et al., 2006, ApJ, 650, 510
Altavilla G. et al., 2004, MNRAS, 349, 1344
Anupama G. C., Sahu D. K., Jose J., 2005, A&A, 429, 667
Arnett W. D., 1982, ApJ, 253, 785
Aubourg É., Tojeiro R., Jimenez R., Heavens A., Strauss M. A., Spergel D. N., 2008, A&A, 492, 631
Axelrod T. S., 1980, PhD thesis, California Univ., Santa Cruz
Betoule M. et al., 2014, A&A, 568, A22
Blinnikov S. I., Khokhlov A. M., 1986, Sov. Astron. Lett., 12, 131
Blondin S. et al., 2012, AJ, 143, 126
Blondin S., Dessart L., Hillier D. J., Khokhlov A. M., 2013, MNRAS, 429, 2127
Blondin S., Dessart L., Hillier D. J., 2015, MNRAS, 448, 2766
Bloom J. S. et al., 2012, ApJ, 744, L17
Branch D., 1992, ApJ, 392, 35
Branch D., Fisher A., Nugent P., 1993, AJ, 106, 2383
Branch D. et al., 2003, AJ, 126, 1489
Brown T. M. et al., 2013, PASP, 125, 1031
Bureau M., Mould J. R., Staveley-Smith L., 1996, ApJ, 463, 60
Buton C. et al., 2013, A&A, 549, A8
Cao Y. et al., 2015, Nature, 521, 328
Cappellari M. et al., 2011, MNRAS, 413, 813
Cappellaro E. et al., 2001, ApJ, 549, L215
Cardelli J. A., Clayton G. C., Mathis J. S., 1989, ApJ, 345, 245
Catinella B., Haynes M. P., Giovanelli R., 2005, AJ, 130, 1037
Chan K.-W., Lingenfelter R. E., 1993, ApJ, 405, 614
Childress M. J. et al., 2013a, ApJ, 770, 29
Childress M. et al., 2013b, ApJ, 770, 107
Childress M. et al., 2013c, ApJ, 770, 108
Childress M. J., Vogt F. P. A., Nielsen J., Sharp R. G., 2014a, Ap&SS, 349, 617
Childress M. J., Filippenko A. V., Ganeshalingam M., Schmidt B. P., 2014b, MNRAS, 437, 338
Childress M. J., Wolf C., Zahid H. J., 2014c, MNRAS, 445, 1898
Chiosi E., Chiosi C., Trevisan P., Piovan L., Orio M., 2015, MNRAS, 448, 2100

Chotard N. et al., 2011, A&A, 529, L4

Churazov E. et al., 2014, Nature, 512, 406

Ciaraldi-Schoolmann F., Seitenzahl I. R., Röpke F. K., 2013, A&A, 559, A117

Colgate S. A., McKee C., 1969, ApJ, 157, 623

Conley A. et al., 2008, ApJ, 681, 482

Contreras C. et al., 2010, AJ, 139, 519

Cortés J. R., Kenney J. D. P., Hardy E., 2008, ApJ, 683, 78

Crawford S. M. et al., 2010, Proc. SPIE, 7737, 773725

Crotts A. P. S., Yourdon D., 2008, ApJ, 689, 1186

D'Andrea C. B. et al., 2011, ApJ, 743, 172

de Vaucouleurs G., de Vaucouleurs A., Corwin H. G., Jr, Buta R. J., Paturel G., Fouqué P., 1991, Third Reference Catalogue of Bright Galaxies. Volume I: Explanations and references. Volume II: Data for galaxies between 0^h and 12^h. Volume III: Data for galaxies between 12^h and 24^h.

Dessart L., Hillier D. J., Blondin S., Khokhlov A., 2014a, MNRAS, 439, 3114

Dessart L., Blondin S., Hillier D. J., Khokhlov A., 2014b, MNRAS, 441, 532

Dessart L., Hillier D. J., Blondin S., Khokhlov A., 2014c, MNRAS, 441, 3249

Diehl R. et al., 2014, Science, 345, 1162

Dilday B. et al., 2012, Science, 337, 942

Dopita M., Hart J., McGregor P., Oates P., Bloxham G., Jones D., 2007, Ap&SS, 310, 255

Dopita M. et al., 2010, Ap&SS, 327, 245

Faber S. M. et al., 2003, in Iye M., Moorwood A. F. M., eds, Proc. SPIE Conf. Ser. Vol. 4841, Instrument Design and Performance for Optical/Infrared Ground-based Telescopes. SPIE, Bellingham, p. 1657

Filippenko A. V. et al., 1992a, AJ, 104, 1543

Filippenko A. V. et al., 1992b, ApJ, 384, L15

Fink M., Röpke F. K., Hillebrandt W., Seitenzahl I. R., Sim S. A., Kromer M., 2010, A&A, 514, A53

Fink M. et al., 2014, MNRAS, 438, 1762

Fisher R., Jumper K., 2015, ApJ, 805, 150

Foley R. J. et al., 2012, ApJ, 753, L5

Foley R. J. et al., 2013, ApJ, 767, 57

Foley R. J. et al., 2014, MNRAS, 443, 2887

Förster F., González-Gaitán S., Folatelli G., Morrell N., 2013, ApJ, 772, 19

Galbany L. et al., 2012, ApJ, 755, 125

Ganeshalingam M. et al., 2010, ApJS, 190, 418

Garavini G. et al., 2004, AJ, 128, 387

Gasques L. R., Afanasjev A. V., Aguilera E. F., Beard M., Chamon L. C., Ring P., Wiescher M., Yakovlev D. G., 2005, Phys. Rev. C, 72, 025806

Gómez G., López R., 1998, AJ, 115, 1096

Graham A. W., Colless M. M., Busarello G., Zaggia S., Longo G., 1998, A&AS, 133, 325

Graham M. L. et al., 2015a, MNRAS, 446, 2073

Graham M. L., Nugent P. E., Sullivan M., Filippenko A. V., Cenko S. B., Silverman J. M., Clubb K. I., Zheng W., 2015b, preprint (arXiv:1502.00646)

Graur O., Zurek D., Shara M. M., Riess A. G., 2015, preprint (arXiv:1505.00777)

Guillochon J., Dan M., Ramirez-Ruiz E., Rosswog S., 2010, ApJ, 709, L64

Gupta R. R. et al., 2011, ApJ, 740, 92

Guy J. et al., 2007, A&A, 466, 11

Guy J. et al., 2010, A&A, 523, A7

Hamuy M. et al., 2003, Nature, 424, 651

Hansen J. E., Raassen A. J. J., Uylings P. H. M., 1984, ApJ, 277, 435

Hayden B. T., Gupta R. R., Garnavich P. M., Mannucci F., Nichol R. C., Sako M., 2013, ApJ, 764, 191

Hicken M. et al., 2009, ApJ, 700, 331

Hicken M. et al., 2012, ApJS, 200, 12

Hillier D. J., Dessart L., 2012, MNRAS, 424, 252

Hoeflich P., Khokhlov A., 1996, ApJ, 457, 500

Hook I. M., Jørgensen I., Allington-Smith J. R., Davies R. L., Metcalfe N., Murowinski R. G., Crampton D., 2004, PASP, 116, 425

Howell D. A. et al., 2006, Nature, 443, 308

Howell D. A. et al., 2009, ApJ, 691, 661

Hoyle F., Fowler W. A., 1960, ApJ, 132, 565

Huo J., Huo S., Dong Y., 2011, Nucl. Data Sheets, 112, 1513

Iben I., Jr, Tutukov A. V., 1984, ApJS, 54, 335

Iben I., Jr, Tutukov A. V., 1991, ApJ, 370, 615

Jeffery D. J., 1999, preprint (astro-ph/9907015)

Jha S. et al., 1999, ApJS, 125, 73

Jha S. et al., 2006, AJ, 131, 527

Johansson J. et al., 2013, MNRAS, 435, 1680

Kasen D., Woosley S. E., 2007, ApJ, 656, 661

Kasen D., Röpke F. K., Woosley S. E., 2009, Nature, 460, 869

Kelly P. L., Hicken M., Burke D. L., Mandel K. S., Kirshner R. P., 2010, ApJ, 715, 743

Kelly P. L., Filippenko A. V., Burke D. L., Hicken M., Ganeshalingam M., Zheng W., 2015, Science, 347, 1459

Kent B. R. et al., 2008, AJ, 136, 713

Kerzendorf W. E., Schmidt B. P., Laird J. B., Podsiadlowski P., Bessell M. S., 2012, ApJ, 759, 7

Kerzendorf W. E. et al., 2013, ApJ, 774, 99

Kerzendorf W. E., Childress M., Scharwächter J., Do T., Schmidt B. P., 2014a, ApJ, 782, 27

Kerzendorf W. E., Taubenberger S., Seitenzahl I. R., Ruiter A. J., 2014b, ApJ, 796, L26

Kessler R. et al., 2009, ApJS, 185, 32

Konishi K. et al., 2011, preprint (arXiv:1101.4269)

Koribalski B. S. et al., 2004, AJ, 128, 16

Kotak R. et al., 2005, A&A, 436, 1021

Krumm N., Salpeter E. E., 1980, AJ, 85, 1312

Kuchner M. J., Kirshner R. P., Pinto P. A., Leibundgut B., 1994, ApJ, 426, L89

Lampeitl H. et al., 2010, ApJ, 722, 566

Landolt A. U., 1992, AJ, 104, 372

Lauberts A., Valentijn E. A., 1989, The Surface Photometry Catalogue of the ESO-Uppsala Galaxies. European Southern Observatory, Garching

Leibundgut B. et al., 1993, AJ, 105, 301

Leloudas G. et al., 2009, A&A, 505, 265

Leonard D. C., 2007, ApJ, 670, 1275

Li W. et al., 2011, Nature, 480, 348

Lira P. et al., 1998, AJ, 115, 234

Livne E., 1990, ApJ, 354, L53

Lorén-Aguilar P., Isern J., García-Berro E., 2010, MNRAS, 406, 2749

Lundqvist P. et al., 2015, A&A, 577, A39

McClelland C. M., Garnavich P. M., Milne P. A., Shappee B. J., Pogge R. W., 2013, ApJ, 767, 119

McCully C. et al., 2014a, Nature, 512, 54

McCully C. et al., 2014b, ApJ, 786, 134

Maeda K. et al., 2010a, Nature, 466, 82

Maeda K., Taubenberger S., Sollerman J., Mazzali P. A., Leloudas G., Nomoto K., Motohara K., 2010b, ApJ, 708, 1703

Maeda K. et al., 2011, MNRAS, 413, 3075

Maguire K. et al., 2012, MNRAS, 426, 2359

Maguire K. et al., 2013, MNRAS, 436, 222

Maguire K. et al., 2014, MNRAS, 444, 3258

Mannucci F., Della Valle M., Panagia N., Cappellaro E., Cresci G., Maiolino R., Petrosian A., Turatto M., 2005, A&A, 433, 807

Mannucci F., Della Valle M., Panagia N., 2006, MNRAS, 370, 773

Marion G. H. et al., 2013, ApJ, 777, 40

Marion G. H. et al., 2015, preprint (arXiv:1507.07261)

Matheson T. et al., 2008, AJ, 135, 1598

Maund J. R. et al., 2010, ApJ, 725, L167

Mazzali P. A., Hachinger S., 2012, MNRAS, 424, 2926

Mazzali P. A., Chugai N., Turatto M., Lucy L. B., Danziger I. J., Cappellaro E., della Valle M., Benetti S., 1997, MNRAS, 284, 151

Mazzali P. A., Cappellaro E., Danziger I. J., Turatto M., Benetti S., 1998, ApJ, 499, L49

Mazzali P. A. et al., 2005, ApJ, 623, L37

Mazzali P. A., Röpke F. K., Benetti S., Hillebrandt W., 2007, Science, 315, 825

Mazzali P. A., Sauer D. N., Pastorello A., Benetti S., Hillebrandt W., 2008, MNRAS, 386, 1897

Mazzali P. A., Maurer I., Stritzinger M., Taubenberger S., Benetti S., Hachinger S., 2011, MNRAS, 416, 881

Mazzali P. A. et al., 2014, MNRAS, 439, 1959

Mazzali P. A. et al., 2015, MNRAS, 450, 2631

Milne P. A., Brown P. J., Roming P. W. A., Bufano F., Gehrels N., 2013, ApJ, 779, 23

Milne P. A., Foley R. J., Brown P. J., Narayan G., 2015, ApJ, 803, 20

Modigliani A. et al., 2010, Proc. SPIE, 7737, 28

Moll R., Raskin C., Kasen D., Woosley S. E., 2014, ApJ, 785, 105

Munari U., Henden A., Belligoli R., Castellani F., Cherini G., Righetti G. L., Vagnozzi A., 2013, New Astron., 20, 30

Nomoto K., 1982, ApJ, 253, 798

Nordsieck K. H., Burgh E. B., Kobulnicky H. A., Williams T. B., O'Donoghue D., Percival J. W., Smith M. P., 2001, BAAS, 33, 1465

Nugent P. E. et al., 2011, Nature, 480, 344

Ogando R. L. C., Maia M. A. G., Pellegrini P. S., da Costa L. N., 2008, AJ, 135, 2424

Olling R. P. et al., 2015, Nature, 521, 332

Pakmor R., Kromer M., Röpke F. K., Sim S. A., Ruiter A. J., Hillebrandt W., 2010, Nature, 463, 61

Pakmor R., Kromer M., Taubenberger S., Springel V., 2013, ApJ, 770, L8

Pan Y.-C., Sullivan M., Maguire K., Gal-Yam A., Hook I. M., Howell D. A., Nugent P. E., Mazzali P. A., 2015a, MNRAS, 446, 354

Pan Y.-C. et al., 2015b, MNRAS, 452, 4307

Pastorello A. et al., 2007, MNRAS, 377, 1531

Patat F. et al., 2007, Science, 317, 924

Pereira R. et al., 2013, A&A, 554, A27

Perlmutter S. et al., 1999, ApJ, 517, 565

Phillips M. M., 1993, ApJ, 413, L105

Phillips M. M., Wells L. A., Suntzeff N. B., Hamuy M., Leibundgut B., Kirshner R. P., Foltz C. B., 1992, AJ, 103, 1632

Pignata G. et al., 2004, MNRAS, 355, 178

Pignata G. et al., 2008, MNRAS, 388, 971

Piro A. L., Nakar E., 2013, ApJ, 769, 67

Piro A. L., Thompson T. A., Kochanek C. S., 2014, MNRAS, 438, 3456

Pisano D. J., Barnes D. G., Staveley-Smith L., Gibson B. K., Kilborn V. A., Freeman K. C., 2011, ApJS, 197, 28

Raskin C., Kasen D., Moll R., Schwab J., Woosley S., 2014, ApJ, 788, 75

Rest A. et al., 2014, ApJ, 795, 44

Richmond M. W., Smith H. A., 2012, J. Am. Assoc. Var. Star Obs., 40, 872

Riess A. G. et al., 1998, AJ, 116, 1009

Riess A. G. et al., 1999, AJ, 117, 707

Riess A. G. et al., 2005, ApJ, 627, 579

Riess A. G. et al., 2011, ApJ, 730, 119

Rigault M. et al., 2013, A&A, 560, A66

Röpke F. K., Niemeyer J. C., 2007, A&A, 464, 683

Röpke F. K. et al., 2012, ApJ, 750, L19

Rothberg B., Joseph R. D., 2006, AJ, 131, 185

Ruiter A. J. et al., 2013, MNRAS, 429, 1425

Ruiz-Lapuente P., Spruit H. C., 1998, ApJ, 500, 360

Sasdelli M., Mazzali P. A., Pian E., Nomoto K., Hachinger S., Cappellaro E., Benetti S., 2014, MNRAS, 445, 711

Savitzky A., Golay M. J. E., 1964, Anal. Chem., 36, 1627

Scalzo R. et al., 2012, ApJ, 757, 12

Scalzo R. et al., 2014a, MNRAS, 440, 1498

Scalzo R. A., Ruiter A. J., Sim S. A., 2014b, MNRAS, 445, 2535

Scannapieco E., Bildsten L., 2005, ApJ, 629, L85

Scarano S., Madsen F. R. H., Roy N., Lépine J. R. D., 2008, MNRAS, 386, 963

Schaefer B. E., Pagnotta A., 2012, Nature, 481, 164

Schmidt B. P., Kirshner R. P., Leibundgut B., Wells L. A., Porter A. C., Ruiz-Lapuente P., Challis P., Filippenko A. V., 1994, ApJ, 434, L19

Schneider S. E., Thuan T. X., Mangum J. G., Miller J., 1992, ApJS, 81, 5

Scolnic D. M., Riess A. G., Foley R. J., Rest A., Rodney S. A., Brout D. J., Jones D. O., 2014, ApJ, 780, 37

Seitenzahl I. R., Taubenberger S., Sim S. A., 2009a, MNRAS, 400, 531

Seitenzahl I. R., Meakin C. A., Townsley D. M., Lamb D. Q., Truran J. W., 2009b, ApJ, 696, 515

Seitenzahl I. R. et al., 2013a, MNRAS, 429, 1156

Seitenzahl I. R., Cescutti G., Röpke F. K., Ruiter A. J., Pakmor R., 2013b, A&A, 559, L5

Shappee B. J., Stanek K. Z., 2011, ApJ, 733, 124

Shappee B. J., Stanek K. Z., Pogge R. W., Garnavich P. M., 2013, ApJ, 762, L5

Shen K. J., Moore K., 2014, ApJ, 797, 46

Silbermann N. A. et al., 1999, ApJ, 515, 1

Silverman J. M. et al., 2012a, MNRAS, 425, 1789

Silverman J. M. et al., 2012b, ApJ, 756, L7

Silverman J. M. et al., 2013a, ApJS, 207, 3

Silverman J. M., Ganeshalingam M., Filippenko A. V., 2013b, MNRAS, 430, 1030

Silverman J. M. et al., 2013c, ApJ, 772, 125

Silverman J. M., Vinkó J., Marion G. H., Wheeler J. C., Barna B., Szalai T., Mulligan B. W., Filippenko A. V., 2015, MNRAS, 451, 1973

Sim S. A., Röpke F. K., Hillebrandt W., Kromer M., Pakmor R., Fink M., Ruiter A. J., Seitenzahl I. R., 2010, ApJ, 714, L52

Sim S. A. et al., 2013, MNRAS, 436, 333

Simon J. D. et al., 2009, ApJ, 702, 1157

Smartt S. J. et al., 2015, A&A, 579, A40

Smith J. A. et al., 2002, AJ, 123, 2121

Sollerman J. et al., 2004, A&A, 428, 555

Spyromilio J., Gilmozzi R., Sollerman J., Leibundgut B., Fransson C., Cuby J.-G., 2004, A&A, 426, 547

Stanishev V. et al., 2007, A&A, 469, 645

Stehle M., Mazzali P. A., Benetti S., Hillebrandt W., 2005, MNRAS, 360, 1231

Strauss M. A., Huchra J. P., Davis M., Yahil A., Fisher K. B., Tonry J., 1992, ApJS, 83, 29

Stritzinger M., Sollerman J., 2007, A&A, 470, L1

Stritzinger M., Leibundgut B., Walch S., Contardo G., 2006a, A&A, 450, 241

Stritzinger M., Mazzali P. A., Sollerman J., Benetti S., 2006b, A&A, 460, 793

Stritzinger M. D. et al., 2011, AJ, 142, 156

Sullivan M. et al., 2006, ApJ, 648, 868

Sullivan M. et al., 2010, MNRAS, 406, 782

Sullivan M. et al., 2011, ApJ, 737, 102

Sunderland A. G., Noble C. J., Burke V. M., Burke P. G., 2002, Comput. Phys. Commun., 145, 311

Suntzeff N. B. et al., 1999, AJ, 117, 1175

Tanaka M., Mazzali P. A., Stanishev V., Maurer I., Kerzendorf W. E., Nomoto K., 2011, MNRAS, 410, 1725

Taubenberger S. et al., 2009, MNRAS, 397, 677

Taubenberger S. et al., 2013, MNRAS, 432, 3117

Taubenberger S. et al., 2015, MNRAS, 448, L48

Theureau G., Bottinelli L., Coudreau-Durand N., Gouguenheim L., Hallet N., Loulergue M., Paturel G., Teerikorpi P., 1998, A&AS, 130, 333

Trager S. C., Faber S. M., Worthey G., González J. J., 2000, AJ, 119, 1645

Tsebrenko D., Soker N., 2015, MNRAS, 447, 2568

Tutukov A. V., Iungelson L. R., 1976, Astrofizika, 12, 521

Tutukov A. V., Yungelson L. R., 1979, Acta Astron., 29, 665

Verheijen M. A. W., Sancisi R., 2001, A&A, 370, 765

Vernet J. et al., 2011, A&A, 536, A105

Wang X., Li W., Filippenko A. V., Foley R. J., Smith N., Wang L., 2008, ApJ, 677, 1060

Wang X. et al., 2009a, ApJ, 697, 380

Wang X. et al., 2009b, ApJ, 699, L139

Wang X., Wang L., Filippenko A. V., Zhang T., Zhao X., 2013, Science, 340, 170

Webbink R. F., 1984, ApJ, 277, 355

Whelan J., Iben I., Jr, 1973, ApJ, 186, 1007

Wong O. I. et al., 2006, MNRAS, 371, 1855

Woosley S. E., Kasen D., 2011, ApJ, 734, 38

Woosley S. E., Weaver T. A., 1994, ApJ, 423, 371

Yamaguchi H. et al., 2015, ApJ, 801, L31
Yaron O., Gal-Yam A., 2012, PASP, 124, 668
Zhang T. et al., 2010, PASP, 122, 1
Zhang J.-J., Wang X.-F., Bai J.-M., Zhang T.-M., Wang B., Liu Z.-W., Zhao
    X.-L., Chen J.-C., 2014, AJ, 148, 1

APPENDIX A: ATOMIC DATA FOR CO III

Rest wavelength: Table A1 lists the transitions in the multiplet of Co III contributing to the 5893 Å feature. Note that the second and third transitions contribute to the main 5893 Å, while other transitions in the multiplet produce other features of interest such as the ~6150 Å feature of Co III (see Fig. 2).

Line emissivity: the [Co III] λ5893 blend accounts for about 70 per cent of the multiplet cooling. Above an electron density of 10^7 cm^{-3} and a temperature of 4000 K, the above multiplet accounts for between 50 and 70 per cent of all cooling by Co III. As the temperature and/or electron density is lowered below these values, cooling via the $3d^7$ a^4F– $3d^7$ a^4P multiplet (with an excitation energy of ~1.9 eV) becomes increasingly important. Plots of the flux in the [Co III] λ5893 blend as a function of electron density and temperature are shown in Fig. A1. The critical density for the $3d^7$ a^2G levels is $\sim 3 \times 10^7$ cm^{-3} and for the $3d^7$ a^4P levels it is $\sim 1 \times 10^6$ cm^{-3}. We note here that collision rates for Co III are unavailable and so we adopted collision strengths from Sunderland et al. (2002) which were computed for Ni IV, and which has a similar electronic structure to Co III.

Table A1. Atomic data for Co III.

Lower level	Upper level	A^a	λ	E (eV)
$3d^7$ $a^4F_{9/2}$	$3d^7$ $a^2G_{7/2}$	0.014	5627.104	2.203
$3d^7$ $a^4F_{9/2}$	$3d^7$ $a^2G_{9/2}$	0.400	5888.482	2.105
$3d^7$ $a^4F_{7/2}$	$3d^7$ $a^2G_{7/2}$	0.150	5906.783	2.203
$3d^7$ $a^4F_{7/2}$	$3d^7$ $a^2G_{9/2}$	0.120	6195.455	2.105
$3d^7$ $a^4F_{5/2}$	$3d^7$ $a^2G_{7/2}$	0.110	6127.670	2.203

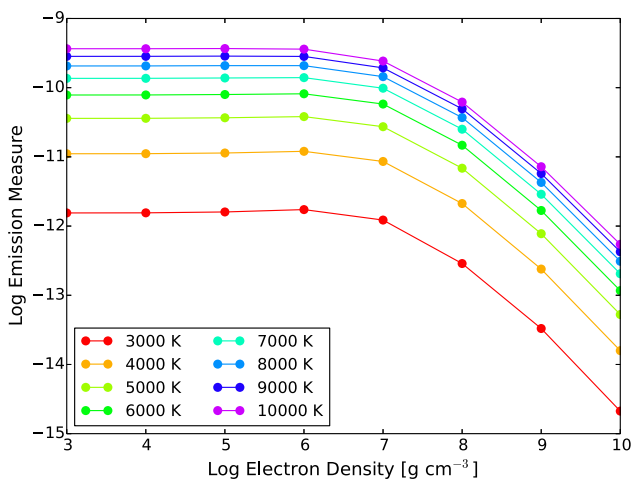*Note.* ^{a}The A values are from Hansen, Raassen & Uylings (1984).

Figure A1. Illustration of the variation of the flux in the [Co III] λ5893 blend with electron density. The different curves are for temperatures of 3000 K (red curve) to 10 000 K (top curve) in steps of 1000 K. For the calculation an SN age of 100 d and a N(Co III) to N(Ne) ratio of 0.01 was assumed. The emission measure has been divided by the product of the electron and Co densities.

APPENDIX B: ANCILLARY DATA ON SN SAMPLE

This appendix presents the properties of SNe Ia and their host galaxies derived in the literature or measured from the data for our analysis.

Table B1 presents the host galaxy distance and redshift information for the SNe Ia in our sample, along with references. As noted in Section 5, distances for SNe Ia in our sample are preferentially derived from Cepheid distances from Riess et al. (2011) where available, and from host redshift with the Riess et al. (2011) Hubble constant value ($H_0 = 73.8$ km s^{-1} Mpc^{-1}). Generally, we avoid other distance indicators such as Tully–Fisher, surface brightness fluctuations, and planetary nebula luminosity functions. The one exception to this is SN 2012cg, for which we use the Cortés, Kenney & Hardy (2008) Tully–Fisher distance modulus, as was done in Silverman et al. (2012b).

For some SNe Ia (SN 2003du, SN 2011by, SN 2013dy), previous analyses in the literature have found that the redshift-based distance modulus yields anomalous values for the SN peak luminosity. Thus, for these we employ SN-based distance moduli adopted by previous authors: the Stritzinger et al. (2006b) value for SN 2003du, the Graham et al. (2015a) value for SN 2011by, and the Pan et al. (2015a) value for SN 2013dy (derived with SNOOPY).

Table B2 presents the pertinent light-curve fit parameters from the main photospheric phase light curves. Light curves were fitted with SiFTO (Conley et al. 2008). For some SNe Ia (SN 2011iv, SN 2011by, SN 2012ht), photometry was not explicitly published, so we utilize the published light-curve widths and colours for these SNe. Where appropriate, we convert $\Delta m_{15}(B)$ or SALT2 $x1$ to SiFTO stretch s using the relations published in Guy et al. (2007, 2010).

Light curves for SN 2013cs and SN 2013gy were obtained with the Las Cumbres Observatory Global Telescope (LCOGT; Brown et al. 2013) and have been reduced using a custom pipeline developed by S. Valenti. The pipeline employs standard procedures (PYRAF, DAOPHOT) in a PYTHON framework. Host galaxy flux was removed using a low-order polynomial background. Point spread function magnitudes were transformed to the standard Sloan Digital Sky Survey (Smith et al. 2002) filter system (for *gri*) or Landolt (1992) system (for *BV*) via standard star observations taken during clear nights. These light curves will be released in a future LCOGT SN programme publication.

Table B3 presents the late-time photometry for our SNe Ia. The *B*-band magnitudes for each phase of spectroscopic observation were determined from a linear fit to the very late ($t \geq 60$ d past peak) *B*-band light curve. Spectra from T15b were already flux calibrated to contemporaneous photometry, so here we report the *B*-band flux synthesized from the spectrum. Similarly, M15 spectra were flux calibrated with spectrophotometric standard stars, and thus are flux calibrated modulo any changes in grey extinction or slit loss between the standard star and SN observation.

For some SNe Ia, sufficient late-time photometry was not available to reliably extrapolate the *B*-band luminosity at the time of spectroscopic observations – generally this occurred if the SN did not have photometry beyond 100 d past peak or if a public light curve was not available. For these SNe, late photometry from an alternate SN was employed, with the requirement that the light-curve stretch be exceptionally close. These SNe with their surrogate light curves are shown in Fig. B1, and the surrogate SN is denoted in the reference column of Table B3.

Table B4 presents the measured [Co III] λ5893 line fluxes, synthesized *B*-band fluxes, and wavelength integration bounds for the

Table B1. Nebular SN Ia host information.

SN	Host name	Host z	Host μ (mag)[a]	μ method	z ref.	μ ref.
SN 1990N	NGC 4639	0.003 395	31.67 ± 0.07	Cepheids	Wong et al. (2006)	Riess et al. (2011)
SN 1991T	NGC 4527	0.005 791	30.72 ± 0.13	Cepheids	Strauss et al. (1992)	NED
SN 1994ae	NGC 3370	0.004 266	32.13 ± 0.07	Cepheids	Krumm & Salpeter (1980)	Riess et al. (2011)
SN 1995D	NGC 2962	0.006 561	32.25 ± 0.33	Redshift	Cappellari et al. (2011)	–
SN 1998aq	NGC 3982	0.003 699	31.70 ± 0.08	Cepheids	de Vaucouleurs et al. (1991)	Riess et al. (2011)
SN 1998bu	NGC 3368	0.002 992	30.20 ± 0.20	Cepheids	de Vaucouleurs et al. (1991)	NED
SN 1999aa	NGC 2595	0.014 443	33.98 ± 0.15	Redshift	de Vaucouleurs et al. (1991)	–
SN 2002cs	NGC 6702	0.015 771	34.17 ± 0.14	Redshift	Trager et al. (2000)	–
SN 2002dj	NGC 5018	0.009 393	33.04 ± 0.23	Redshift	Rothberg & Joseph (2006)	–
SN 2002er	UGC 10743	0.008 569	32.84 ± 0.25	Redshift	de Vaucouleurs et al. (1991)	–
SN 2002fk	NGC 1309	0.007 125	32.59 ± 0.09	Cepheids	Koribalski et al. (2004)	Riess et al. (2011)
SN 2003du	UGC 9391	0.006 384	32.75 ± 0.20	SN	Schneider et al. (1992)	Stritzinger et al. (2006b)
SN 2003hv	NGC 1201	0.005 624	31.92 ± 0.39	Redshift	Ogando et al. (2008)	–
SN 2004bv	NGC 6907	0.010 614	33.31 ± 0.20	Redshift	Scarano et al. (2008)	–
SN 2004eo	NGC 6928	0.015 701	34.16 ± 0.14	Redshift	Theureau et al. (1998)	–
SN 2005cf	MCG-01-39-3	0.006 430	32.21 ± 0.34	Redshift	Childress et al. (2013b)	–
SN 2007af	NGC 5584	0.005 464	31.72 ± 0.07	Cepheids	Koribalski et al. (2004)	Riess et al. (2011)
SN 2007gi	NGC 4036	0.004 620	31.49 ± 0.47	Redshift	Cappellari et al. (2011)	–
SN 2007le	NGC 7721	0.006 721	32.31 ± 0.32	Redshift	Koribalski et al. (2004)	–
SN 2007sr	NGC 4038	0.005 477	31.66 ± 0.08	Cepheids	Lauberts & Valentijn (1989)	Riess et al. (2011)
SN 2009le	MCG-04-06-9	0.017 786	34.44 ± 0.12	Redshift	Theureau et al. (1998)	–
SN 2011by	NGC 3972	0.002 843	32.01 ± 0.07	SN	Verheijen & Sancisi (2001)	Graham et al. (2015a)
SN 2011fe	NGC 5457	0.000 804	29.05 ± 0.06	Cepheids	de Vaucouleurs et al. (1991)	Shappee & Stanek (2011)
SN 2011iv	NGC 1404	0.006 494	32.23 ± 0.33	Redshift	Graham et al. (1998)	–
SN 2012cg	NGC 4424	0.001 458	30.90 ± 0.30	TF	Kent et al. (2008)	Cortés et al. (2008)
SN 2012fr	NGC 1365	0.005 457	31.31 ± 0.20	Cepheids	Bureau, Mould & Staveley-Smith (1996)	Silbermann et al. (1999)
SN 2012hr	ESO 121-G026	0.007 562	32.56 ± 0.29	Redshift	Koribalski et al. (2004)	–
SN 2013aa	NGC 5643	0.003 999	31.18 ± 0.54	Redshift	Koribalski et al. (2004)	–
SN 2013cs	ESO 576-G017	0.009 243	33.00 ± 0.24	Redshift	Pisano et al. (2011)	–
SN 2013dy	NGC 7250	0.003 889	31.49 ± 0.10	SN	Schneider et al. (1992)	Pan et al. (2015a)
SN 2013gy	NGC 1418	0.014 023	33.92 ± 0.15	Redshift	Catinella, Haynes & Giovanelli (2005)	–
SN 2014J	NGC 3034	0.000 677	27.60 ± 0.10	Cepheids+SN	de Vaucouleurs et al. (1991)	Foley et al. (2014)

Note. [a]For hosts with redshift-based μ, uncertainty includes a peculiar velocity term of 300 km s^{-1}.

Table B2. Light-curve fit results and sources.

SN	MJD of B_{max}	Rest frame B_{max} (mag)	Stretch	Colour c	LC ref.
SN 1990N	48081.69	12.706 ± 0.015	1.081 ± 0.012	0.049 ± 0.013	Lira et al. (1998)
SN 1991T	48373.95	11.468 ± 0.028	1.047 ± 0.019	0.101 ± 0.026	Lira et al. (1998)
SN 1994ae	49684.56	12.968 ± 0.019	1.057 ± 0.014	−0.060 ± 0.016	CfA
SN 1995D	49767.50	13.273 ± 0.025	1.097 ± 0.014	−0.006 ± 0.015	CfA
SN 1998aq	50930.24	12.316 ± 0.009	0.965 ± 0.010	−0.146 ± 0.009	Riess et al. (2005)
SN 1998bu	50952.06	12.118 ± 0.013	0.962 ± 0.018	0.270 ± 0.010	Jha et al. (1999), Suntzeff et al. (1999)
SN 1999aa	51231.84	14.755 ± 0.016	1.134 ± 0.009	−0.047 ± 0.009	CfA
SN 2002cs	52409.24	15.138 ± 0.039	1.007 ± 0.013	0.017 ± 0.016	LOSS
SN 2002dj	52450.32	13.974 ± 0.035	0.962 ± 0.013	0.098 ± 0.016	LOSS
SN 2002er	52524.03	14.267 ± 0.057	0.901 ± 0.009	0.123 ± 0.018	LOSS
SN 2002fk	52547.28	13.152 ± 0.017	0.995 ± 0.012	−0.142 ± 0.012	LOSS
SN 2003du	52765.48	13.476 ± 0.007	1.016 ± 0.008	−0.110 ± 0.008	LOSS
SN 2003hv	52891.12	12.444 ± 0.020	0.741 ± 0.021	−0.115 ± 0.014	Leloudas et al. (2009)
SN 2004bv	53159.83	13.938 ± 0.024	1.146 ± 0.014	0.122 ± 0.013	LOSS
SN 2004eo	53277.66	15.099 ± 0.038	0.863 ± 0.009	0.002 ± 0.014	CSP
SN 2005cf	53533.28	13.625 ± 0.035	0.968 ± 0.009	0.021 ± 0.013	LOSS
SN 2007af	54173.88	13.180 ± 0.015	0.955 ± 0.011	0.058 ± 0.010	CSP
SN 2007gi	54327.66	13.158 ± 0.016	0.871 ± 0.013	0.097 ± 0.017	Zhang et al. (2010)

Table B2. – *Continued.*

SN	MJD of B_{max}	Rest frame B_{max} (mag)	Stretch	Colour c	LC ref.
SN 2007le	54398.62	13.876 ± 0.016	1.028 ± 0.015	0.342 ± 0.014	CSP
SN 2007sr	54448.70	12.809 ± 0.042	0.970 ± 0.031	0.141 ± 0.016	LOSS
SN 2009le	55165.16	15.351 ± 0.030	1.022 ± 0.022	0.079 ± 0.033	CfA
SN 2011by	55690.60	12.890 ± 0.030	0.959 ± 0.019	0.000 ± 0.050	Graham et al. (2015a)
SN 2011fe	55814.51	9.940 ± 0.010	0.969 ± 0.010	-0.066 ± 0.021	Pereira et al. (2013)
SN 2011iv	55906.00	12.530 ± 0.040	0.684 ± 0.020	0.000 ± 0.050	Foley et al. (2012)
SN 2012cg	56082.03	12.128 ± 0.011	1.063 ± 0.011	0.184 ± 0.010	Munari et al. (2013), Marion et al. (2015)
SN 2012fr	56243.68	12.017 ± 0.013	1.108 ± 0.008	0.059 ± 0.011	Zhang et al. (2014)
SN 2012hr	56289.20	13.780 ± 0.020	1.018 ± 0.021	0.030 ± 0.010	Maguire et al. (2013)
SN 2013aa	56344.00	11.330 ± 0.050	1.146 ± 0.019	-0.050 ± 0.010	Maguire et al. (2013)
SN 2013cs	56436.95	13.659 ± 0.032	1.006 ± 0.010	0.054 ± 0.015	LCOGT
SN 2013dy	56500.65	12.824 ± 0.048	1.101 ± 0.007	0.195 ± 0.015	Pan et al. (2015b)
SN 2013gy	56648.61	14.742 ± 0.020	0.948 ± 0.008	0.070 ± 0.011	LCOGT
SN 2014J	56689.74	11.850 ± 0.012	1.086 ± 0.010	1.251 ± 0.012	Foley et al. (2014)

Notes. CfA: Riess et al. (1999), Jha et al. (2006), Hicken et al. (2009, 2012); LOSS: Ganeshalingam et al. (2010); CSP: Contreras et al. (2010), Stritzinger et al. (2011).

Table B3. Late-phase photometry.

SN	Phase t (d)	Obs. date	$m_B(t)$ (mag)	Phot. ref.
SN 1990N	160	19901217	17.394 ± 0.014	Lira et al. (1998)
SN 1990N	186	19910112	17.760 ± 0.011	
SN 1990N	227	19910222	18.337 ± 0.007	
SN 1990N	255	19910322	18.731 ± 0.008	
SN 1990N	280	19910416	19.083 ± 0.011	
SN 1990N	333	19910608	19.829 ± 0.018	
SN 1991T	186	19911031	17.614 ± 0.024	Schmidt et al. (1994)
SN 1991T	258	19920111	18.194 ± 0.018	
SN 1991T	320	19920313	18.694 ± 0.018	
SN 1991T	349	19920411	18.928 ± 0.019	
SN 1994ae	144	19950422	17.672 ± 0.025	Altavilla et al. (2004)
SN 1994ae	153	19950501	17.812 ± 0.027	
SN 1995D	277	19951124	19.887 ± 0.041	Altavilla et al. (2004)
SN 1995D	285	19951202	20.001 ± 0.043	
SN 1998aq	211	19981124	18.140 ± 0.011	Riess et al. (2005)
SN 1998aq	231	19981214	18.442 ± 0.013	
SN 1998aq	241	19981224	18.593 ± 0.013	
SN 1998bu	179	19981114	17.202 ± 0.017	**SN 2011fe**
SN 1998bu	190	19981125	17.347 ± 0.019	
SN 1998bu	208	19981213	17.586 ± 0.022	
SN 1998bu	217	19981222	17.705 ± 0.023	
SN 1998bu	236	19990110	17.956 ± 0.026	
SN 1998bu	243	19990117	18.049 ± 0.028	
SN 1998bu	280	19990223	18.538 ± 0.034	
SN 1998bu	329	19990413	19.187 ± 0.042	
SN 1998bu	340	19990424	19.332 ± 0.043	
SN 1999aa	256	19991109	20.872 ± 0.000	**SN 1991T**
SN 1999aa	282	19991205	21.236 ± 0.000	
SN 2002cs	174	20021106	20.264 ± 0.080	LOSS
SN 2002dj	222	20030201	20.143 ± 0.058	Pignata et al. (2004)
SN 2002dj	275	20030326	21.003 ± 0.040	
SN 2002er	216	20030410	20.429 ± 0.022	Pignata et al. (2008)
SN 2002fk	150	20030227	18.099 ± 0.024	CfA, LOSS

Table B3. – *continued.*

SN	Phase t (d)	Obs. date	$m_B(t)$ (mag)	Phot. ref.
SN 2003du	209	20031201	19.096 ± 0.004	Stanishev et al. (2007)
SN 2003du	221	20031213	19.274 ± 0.004	
SN 2003du	272	20040202	20.031 ± 0.005	
SN 2003du	377	20040517	21.589 ± 0.008	
SN 2003hv	323	20040725	20.870 ± 0.012	Leloudas et al. (2009)
SN 2004bv	171	20041114	18.713 ± 0.000	**SN 1991T**
SN 2004eo	228	20050516	21.454 ± 0.008	Pastorello et al. (2007)
SN 2005cf	319	20060427	20.558 ± 0.040	**SN 2011fe**
SN 2007af	151	20070807	17.816 ± 0.012	**SN 2011fe**
SN 2007af	165	20070821	18.002 ± 0.014	
SN 2007af	308	20080111	19.894 ± 0.037	
SN 2007gi	161	20080115	17.920 ± 0.014	Zhang et al. (2010)
SN 2007le	317	20080827	20.653 ± 0.000	**SN 1991T**
SN 2007sr	177	20080623	17.994 ± 0.021	CfA, LOSS
SN 2009le	324	20101016	22.651 ± 0.050	CfA
SN 2011by	206	20111202	18.337 ± 0.022	**SN 2011fe**
SN 2011by	310	20120315	19.713 ± 0.039	
SN 2011fe	196	20120324	15.238 ± 0.019	Richmond & Smith (2012)
SN 2011fe	230	20120427	15.686 ± 0.024	
SN 2011fe	276	20120612	16.292 ± 0.030	
SN 2011fe	314	20120720	16.792 ± 0.036	
SN 2011iv	318	20121024	20.717 ± 0.050	T15b
SN 2012cg	330	20130507	19.824 ± 0.085	**SN 1994ae**
SN 2012cg	342	20130513	19.917 ± 0.087	
SN 2012fr	151	20130412	16.466 ± 0.034	Zhang et al. (2014)
SN 2012fr	222	20130622	17.560 ± 0.065	
SN 2012fr	261	20130731	18.161 ± 0.082	
SN 2012fr	340	20131018	19.379 ± 0.117	
SN 2012fr	357	20131103	19.409 ± 0.100	
SN 2012fr	357	20131103	19.625 ± 0.124	
SN 2012fr	367	20131114	19.795 ± 0.129	
SN 2012hr	283	20131006	20.487 ± 0.005	**SN 2003du**
SN 2012hr	368	20131230	21.749 ± 0.007	
SN 2013aa	185	20130827	16.438 ± 0.000	**SN 1991T**
SN 2013aa	202	20130913	16.676 ± 0.000	
SN 2013aa	342	20140131	18.633 ± 0.001	
SN 2013aa	358	20140216	18.857 ± 0.001	
SN 2013aa	430	20140422	19.765 ± 0.001	
SN 2013cs	322	20140324	20.939 ± 0.069	**SN 2002fk**
SN 2013cs	322	20140324	21.475 ± 0.100	
SN 2013dy	333	20140626	20.716 ± 0.033	Pan et al. (2015a)
SN 2013dy	419	20140920	22.064 ± 0.045	
SN 2013gy	276	20140920	21.242 ± 0.062	**SN 2011fe**
SN 2014J	231	20140920	16.956 ± 0.119	Foley et al. (2014)

Note. For SNe with poor late-time photometric coverage, the late light curve of a surrogate SN (denoted in boldface in the Photometry Reference column) is employed.
CfA: Riess et al. (1999), Jha et al. (2006), Hicken et al. (2009, 2012); LOSS: Ganeshalingam et al. (2010); CSP: Contreras et al. (2010), Stritzinger et al. (2011).
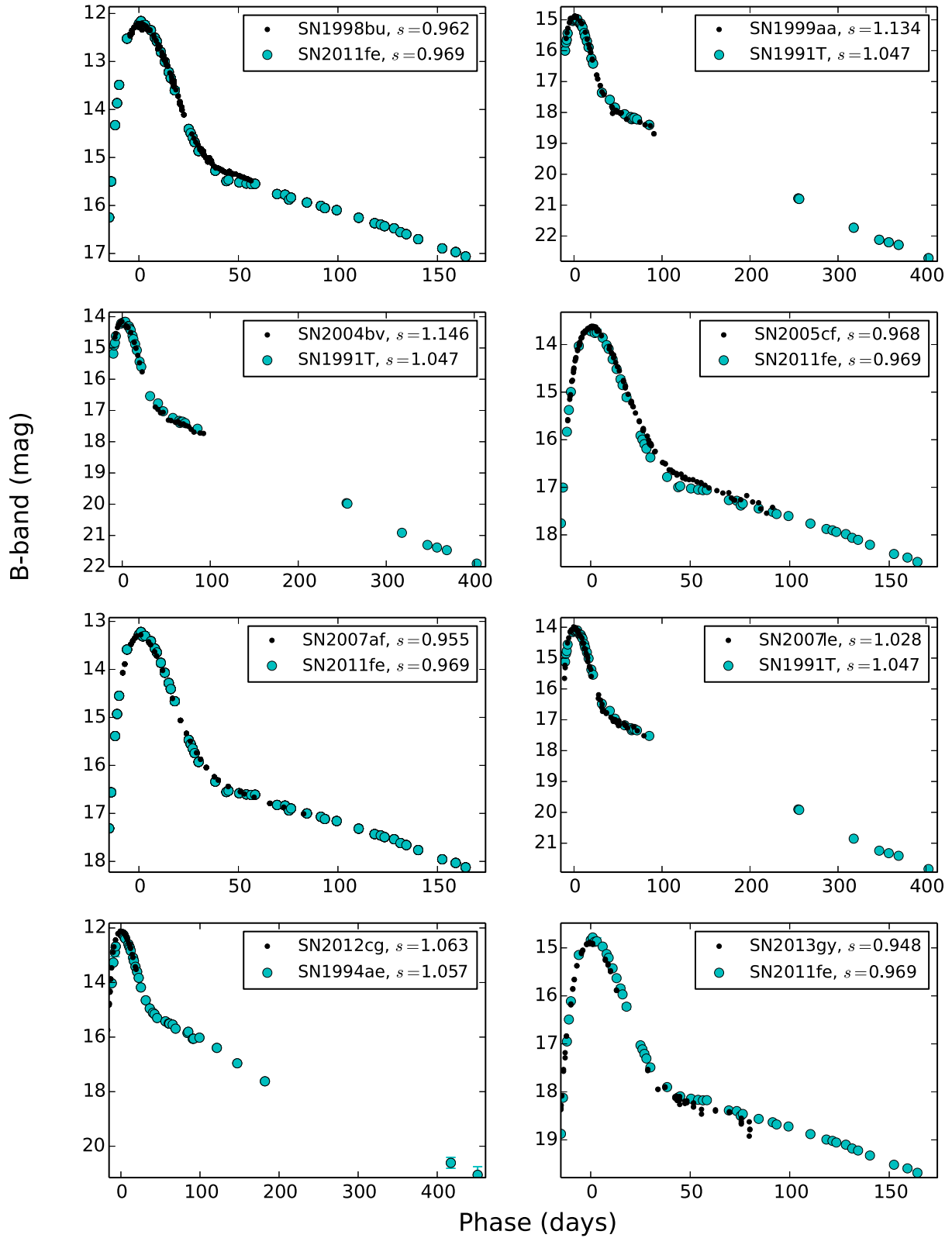
Figure B1. Surrogate light curves for SNe Ia with poor late-time light-curve coverage. Original SN data are shown as small black dots while surrogate SN data are shown as larger blue circles.

Table B4. Co line fluxes from spectra.

SN	Date	Log (Co line flux) $+17$ (erg cm^2 s^{-1})	Spectrum rescale[a]	w_{min} (Å)	w_{max} (Å)
SN 1990N	19901217	1.783 ± 0.002	189.891	5710.5	6038.4
SN 1990N	19910112	3.777 ± 0.000	1.198		
SN 1990N	19910222	3.567 ± 0.001	0.848		
SN 1990N	19910322	2.990 ± 0.002	1.524		
SN 1990N	19910416	2.855 ± 0.003	1.368		
SN 1990N	19910608	2.276 ± 0.011	1.327		
SN 1991T	19911031	2.126 ± 0.007	66.503	5664.2	6121.0
SN 1991T	19920111	3.740 ± 0.001	0.700		
SN 1991T	19920313	1.071 ± 0.016	185.419		
SN 1991T	19920411	0.753 ± 0.019	195.376		
SN 1994ae	19950422	1.829 ± 0.005	137.308	5747.5	6027.4
SN 1994ae	19950501	3.731 ± 0.001	1.124		
SN 1995D	19951124	2.695 ± 0.031	1.378	5677.7	6080.5
SN 1995D	19951202	2.292 ± 0.038	2.270		
SN 1998aq	19981124	3.580 ± 0.014	1.255	5668.6	6077.6
SN 1998aq	19981214	3.771 ± 0.004	0.695		
SN 1998aq	19981224	3.687 ± 0.006	0.574		
SN 1998bu	19981114	4.103 ± 0.002	1.488	5706.7	6055.0
SN 1998bu	19981125	4.144 ± 0.002	1.082		
SN 1998bu	19981213	3.942 ± 0.002	1.090		
SN 1998bu	19981222	3.905 ± 0.004	1.182		
SN 1998bu	19990110	1.661 ± 0.001	107.206		
SN 1998bu	19990117	3.738 ± 0.003	1.237		
SN 1998bu	19990223	1.317 ± 0.003	135.238		
SN 1998bu	19990413	2.814 ± 0.005	2.130		
SN 1998bu	19990424	1.152 ± 0.008	108.216		
SN 1999aa	19991109	1.256 ± 0.003	31.221	5616.9	6197.1
SN 1999aa	19991205	0.858 ± 0.005	56.034		
SN 2002cs	20021106	1.128 ± 0.002	78.636	5655.5	6097.2
SN 2002dj	20030326	2.533 ± 0.003	1.040	5678.4	6148.5
SN 2002er	20030410	2.701 ± 0.008	0.977	5709.1	6086.8
SN 2002fk	20030227	1.695 ± 0.001	113.251	5739.0	6008.7
SN 2003du	20031201	3.144 ± 0.004	1.323	5736.0	6027.0
SN 2003du	20031213	2.950 ± 0.005	1.243		
SN 2003du	20040202	2.524 ± 0.008	0.882		
SN 2003du	20040517	1.703 ± 0.007	1.132		
SN 2003hv	20040725	2.337 ± 0.003	0.907	5687.6	6061.5
SN 2004bv	20041114	1.590 ± 0.001	99.174	5744.3	6057.6
SN 2004eo	20050516	2.166 ± 0.001	1.305	5737.5	6034.0
SN 2005cf	20060427	-0.353 ± 0.020	678.728	5764.7	5992.4
SN 2007af	20070807	1.397 ± 0.006	271.437	5762.2	6027.6
SN 2007af	20070821	1.553 ± 0.005	177.416		
SN 2007af	20080111	2.341 ± 0.009	2.166		
SN 2007gi	20080115	2.079 ± 0.001	80.968	5706.8	6146.6
SN 2007le	20080827	0.254 ± 0.011	164.046	5721.8	6087.5
SN 2007sr	20080623	3.646 ± 0.001	1.258	5765.7	6059.7
SN 2009le	20101016	1.714 ± 0.008	1.000	5587.7	6195.9
SN 2011by	20111202	2.268 ± 0.001	18.360	5723.6	6039.5
SN 2011by	20120315	0.766 ± 0.003	90.491		
SN 2011fe	20120324	4.331 ± 0.000	2.693	5738.3	6027.2
SN 2011fe	20120427	3.919 ± 0.000	3.601		
SN 2011fe	20120612	3.755 ± 0.000	2.189		
SN 2011fe	20120720	3.451 ± 0.001	2.210		
SN 2011iv	20121024	2.443 ± 0.006	1.000	5693.8	6089.2
SN 2012cg	20130507	2.600 ± 0.006	1.344	5698.9	6113.3
SN 2012cg	20130513	2.634 ± 0.004	1.004		
SN 2012fr	20130412	4.346 ± 0.003	1.053	5759.2	6061.5
SN 2012fr	20130622	3.546 ± 0.005	1.604		

Table B4. – *continued.*

SN	Date	Log (Co line flux) +17 (erg cm^2 s^{-1})	Spectrum rescale[a]	w_{min} (Å)	w_{max} (Å)
SN 2012fr	20130731	3.118 ± 0.005	1.864		
SN 2012fr	20131018	2.516 ± 0.014	1.598		
SN 2012fr	20131103	2.738 ± 0.000	0.878		
SN 2012fr	20131114	2.098 ± 0.036	1.757		
SN 2012hr	20131006	0.557 ± 0.003	72.467	5775.3	6041.1
SN 2013aa	20130827	3.769 ± 0.001	3.891	5720.3	6055.9
SN 2013aa	20130913	3.815 ± 0.003	2.524		
SN 2013aa	20140131	2.246 ± 0.037	4.059		
SN 2013aa	20140216	2.322 ± 0.006	4.588		
SN 2013aa	20140422	1.920 ± 0.014	4.680		
SN 2013cs	20140324	2.000 ± 0.008	1.638	5735.8	6061.7
SN 2013dy	20140626	2.744 ± 0.003	0.498	5636.9	6168.7
SN 2013dy	20140920	3.162 ± 0.004	0.090		
SN 2013gy	20140920	2.882 ± 0.003	0.337	5726.8	6064.7
SN 2014J	20140920	5.218 ± 0.002	0.193	5737.8	6069.5

Note. [a]Factor applied to spectrum to enforce consistency with observed *B*-band magnitude.

[Co III] λ5893 flux measurements. Note that the fluxes in this table are in the natural units of the spectroscopic data, as measured from its publicly available format.

[1]*Research School of Astronomy and Astrophysics, Australian National University, Canberra, ACT 2611, Australia*
[2]*ARC Centre of Excellence for All-sky Astrophysics (CAASTRO), Australia*
[3]*Department of Physics and Astronomy & Pittsburgh Particle Physics, Astrophysics, and Cosmology Center (PITT PACC), University of Pittsburgh, 3941 O'Hara Street, Pittsburgh, PA 15260, USA*
[4]*School of Physics and Astronomy, University of Southampton, Southampton SO17 1BJ, UK*
[5]*European Organisation for Astronomical Research in the Southern Hemisphere (ESO), Karl-Schwarzschild-Str. 2, D-85748 Garching b. München, Germany*
[6]*Institute of Astronomy, University of Cambridge, Madingley Rd., Cambridge CB3 0HA, UK*
[7]*Department of Physics, Lehigh University, 16 Memorial Drive East, Bethlehem, PA 18015, USA*
[8]*Department of Physics and Astronomy, Rutgers, the State University of New Jersey, 136 Frelinghuysen Road, Piscataway, NJ 08854, USA*
[9]*INAF – Osservatorio Astronomico di Padova, vicolo dell'Osservatorio 5, I-35122 Padova, Italy*
[10]*Department of Particle Physics and Astrophysics, The Weizmann Institute of Science, Rehovot 76100, Israel*
[11]*Department of Astronomy, University of California, Berkeley, CA 94720-3411, USA*
[12]*Department of Physics, University of California, Broida Hall, Mail Code 9530, Santa Barbara, CA 93106-9530, USA*
[13]*Las Cumbres Observatory Global Telescope Network, 6740 Cortona Dr., Suite 102, Goleta, CA 93117, USA*
[14]*Astrophysics Research Centre, School of Mathematics and Physics, Queen's University Belfast, Belfast BT7 1NN, UK*
[15]*Astrophysics Research Institute, Liverpool John Moores University, Egerton Wharf, Birkenhead, CH41 1LD, UK*
[16]*Max-Planck-Institut für Astrophysik, Karl-Schwarzschild Str. 1, D-85748 Garching, Germany*
[17]*Institut de Ciències de l'Espai (CSIC-IEEC), Campus UAB, Camí de Can Magrans S/N, E-08193 Cerdanyola, Spain*
[18]*Department of Astrophysical Sciences, Princeton University, Princeton, NJ 08544, USA*
[19]*The Oskar Klein Centre, Department of Astronomy, AlbaNova, Stockholm University, 10691 Stockholm, Sweden*

This paper has been typeset from a TEX/LATEX file prepared by the author.